Article

Current Biology

Sub-second fluctuations between top-down and bottom-up modes distinguish diverse human brain states

Highlights

- Relative phase analysis tracks whole-brain phase directionality in real time
- Top-down and bottom-up modes alternate approximately every 200 ms
- Directional modes weaken with anesthesia and recover with consciousness
- EEG-fMRI and ADHD data link phase directionality to brain-state function

Authors

Youngjai Park, Younghwa Cha, Hyoungkyu Kim, ..., Seok-Jun Hong, Christopher J. Honey, Joon-Young Moon

Correspondence

joon.young.moon@gmail.com

In brief

Park et al. introduce relative phase analysis, a real-time framework for tracking whole-brain phase directionality. They show that human brain activity alternates between top-down and bottom-up modes approximately every 200 ms. These dynamics weaken under anesthesia, are altered in ADHD, and align with large-scale functional brain networks.

Park et al., 2026, Current Biology *36*, 3548–3565
July 20, 2026
https://doi.org/10.1016/j.cub.2026.06.014

CellPress

CellPress

Current Biology

Article

Sub-second fluctuations between top-down and bottom-up modes distinguish diverse human brain states

Youngjai Park,[1,2,14] Younghwa Cha,[1,2,3,4,14] Hyoungkyu Kim,[1,2,3,14] Yukyung Kim,[1,2] Jae Hyung Woo,[5] Jehyeop Lee,[1,2] Hanbyul Cho,[1,2] George A. Mashour,[6,7,8] Ting Xu,[9] UnCheol Lee,[6,7,8] Seok-Jun Hong,[1,9,10,11,12] Christopher J. Honey,[13] and Joon-Young Moon[1,2,15,16,*]

[1]Center for Neuroscience Imaging Research, Institute for Basic Science, Suwon 16419, Republic of Korea
[2]Sungkyunkwan University, Suwon 16419, Republic of Korea
[3]Research Institute of Slowave Inc., Seoul 06160, Republic of Korea
[4]Department of Biobehavioral Health, Pennsylvania State University, University Park, PA 16802, USA
[5]Department of Psychological and Brain Sciences, Dartmouth College, Hanover, NH 03755, USA
[6]Department of Anesthesiology, University of Michigan Medical School, Ann Arbor, MI 48109, USA
[7]Center for Consciousness Science, University of Michigan Medical School, Ann Arbor, MI 48109, USA
[8]Neuroscience Graduate Program, University of Michigan, Ann Arbor, MI 48109, USA
[9]Center for the Developing Brain, Child Mind Institute, New York, NY 10022, USA
[10]Department of Biomedical Engineering, Sungkyunkwan University, Suwon 16419, Republic of Korea
[11]Department of Intelligent Precision Healthcare Convergence, Sungkyunkwan University, Suwon 16419, Republic of Korea
[12]Department of MetaBioHealth, Sungkyunkwan University, Suwon 16419, Republic of Korea
[13]Department of Psychological and Brain Sciences, Johns Hopkins University, Baltimore, MD 21218, USA
[14]These authors contributed equally
[15]Present address: Department of Data Science, Hanyang University, 04763 Seoul, Republic of Korea
[16]Lead contact
*Correspondence: joon.young.moon@gmail.com
https://doi.org/10.1016/j.cub.2026.06.014

SUMMARY

Information continuously flows between regions of the human brain, forming patterns that shift across states of consciousness, cognitive modes, and neuropsychiatric conditions. While functional magnetic resonance imaging (fMRI) reveals large-scale activity changes over seconds, the electrophysiological dynamics governing sub-second reconfiguration remain poorly understood. Here, relative phase analysis (RPA), a method leveraging phase lead/lag relationships, is introduced to capture whole-brain dynamics with millisecond precision in real time from electroencephalography (EEG). RPA reveals sub-second alternations, occurring approximately every 200 ms, between two dominant modes of information flow: a top-down mode, where anterior regions drive posterior activity, and a bottom-up mode, characterized by reverse directionality. These dynamics are most prominent during wakefulness, gradually diminish under anesthesia, and exhibit pathological imbalance in attention-deficit/hyperactivity disorder (ADHD). Simultaneous EEG-fMRI recordings demonstrate that top-down dynamics coincide with increased activity of higher-order cognitive networks, whereas bottom-up dynamics correspond to heightened activity in sensory networks. A connectome-based coupled-oscillator model reproduces these transitions, indicating that sub-second fluctuations emerge naturally from inter-regional interactions shaped by underlying structural connectivity. This study establishes RPA as a framework for tracking whole-brain dynamics precisely in real time and identifies sub-second top-down/bottom-up alternations as a fundamental organizing principle of human brain function and consciousness.

INTRODUCTION

Information continuously flows between distinct regions of the human brain,[1–13] forming characteristic patterns that dynamically reconfigure across states of consciousness,[1,4,5] cognitive modes,[3,11,12] and neuropsychiatric conditions,[14–17] and understanding these patterns is essential for unraveling the neural mechanisms underlying the multifaceted nature of human behavior.

A key challenge in neuroscience is to reliably capture and interpret the directionality of information flow across distributed brain regions. In this context, the distinction between top-down and bottom-up signaling has emerged as a central framework for understanding inter-regional communication.[3,9–11,18] Top-down signals from higher-order cognitive areas modulate sensory processing and support goal-directed behavior, whereas bottom-up signals from sensory cortices underpin encoding of environmental stimuli. Owing to limited temporal resolution, fMRI

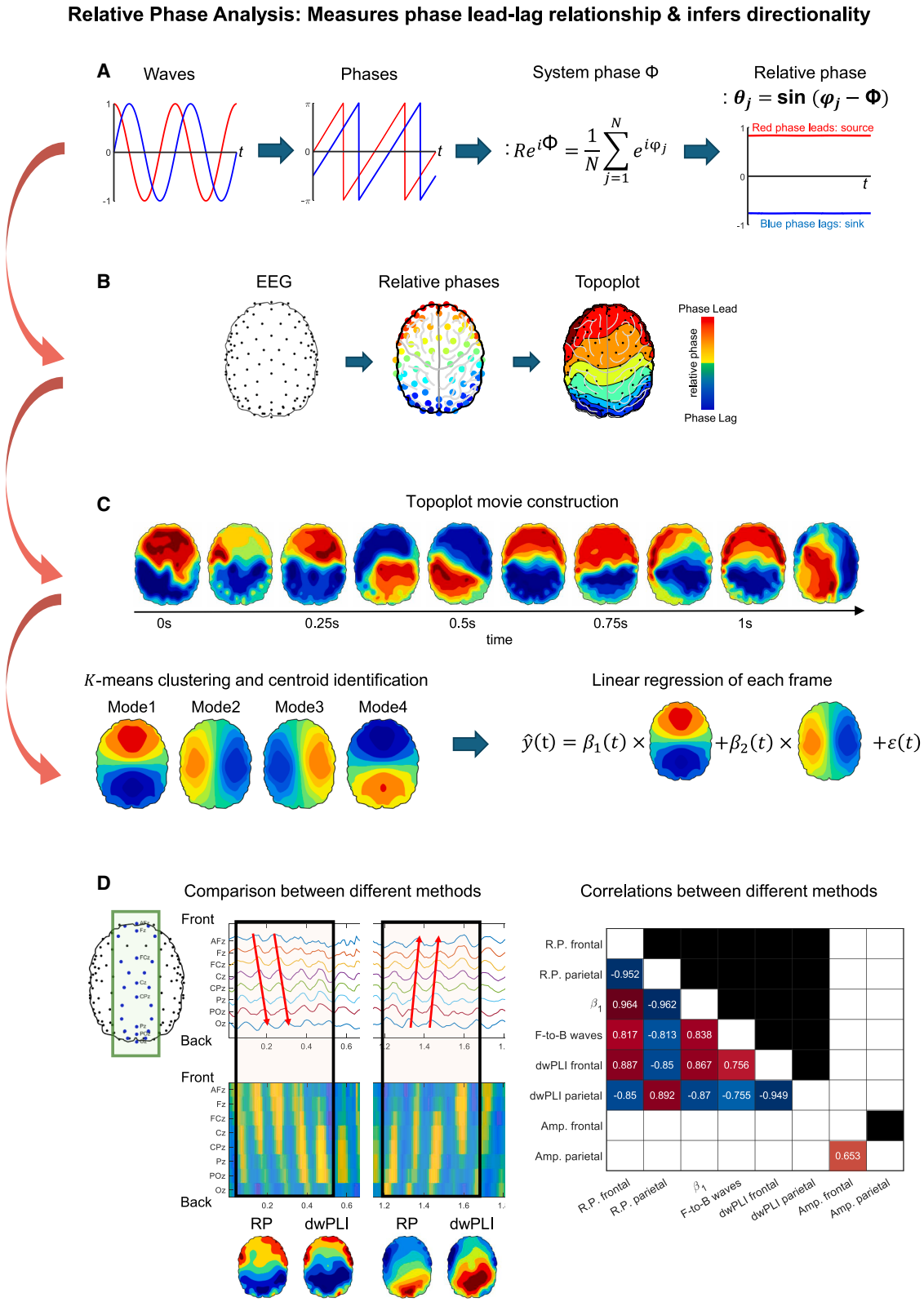

Figure 1. Schematics of RPA

(A) After Hilbert-transforming the EEG time series to extract instantaneous phase, the global system phase Φ is computed by averaging all channel phases; the relative phase of channel j is $\sin(\varphi_j - \Phi)$, mapped continuously from -1 (90° lag) to $+1$ (90° lead).

(legend continued on next page)

studies have primarily examined functional networks associated with these directional processes.[3,18–21] Nevertheless, recent fMRI research has revealed spontaneous blood oxygenation level-dependent (BOLD) fluctuations forming organized spatio-temporal patterns, including traveling waves.[22–24] In contrast, electroencephalography (EEG) and electrocorticography (ECoG) studies—leveraging superior temporal resolution—have more directly probed directional flow and its association with cognitive processes.[5,7,9,10,12] Still, the real-time dynamics of transitions between these directional modes remain largely elusive: how do dominant patterns shift in real time, and can these transition dynamics, observed in brain waves, be systematically linked to functional networks derived from BOLD activity?

Traditional measures of electrocortical signals—such as traveling-wave propagation[8–12] and phase-based indices[25,26]—have provided valuable insights into inter-regional directionality. Phase-based indices estimate the likelihood that one signal consistently leads or lags another over defined time windows, capturing asymmetric interactions in a time-averaged manner.[5,7,26] Traveling-wave analyses typically track neural activity propagation in selected brain regions and have been linked to cognitive functions involving top-down and bottom-up processing.[10–12] Fast switching between directional modes may be particularly relevant for cognitive processing because cortical communication has been suggested to operate through transient sub-second sampling and reconfiguration cycles. Rhythmic perceptual and attentional sampling has been reported across the ~3–12 Hz (~83–333 ms) range,[27] whereas magnetoencephalography (MEG) studies show that large-scale electrophysiological network configurations can transiently reorganize and be expressed over ~100–200 ms.[28]

Here, we introduce a new framework, relative phase analysis (RPA), that captures top-down and bottom-up modes and the transitions between them. By leveraging phase-lead/lag relationships in brain waves, RPA provides a robust method to track real-time, whole-brain directionality pattern dynamics. We show that the brain alternates between two dominant global modes approximately every 200 ms: a top-down mode, where anterior regions phase lead posterior ones, and a bottom-up mode, where posterior regions lead anterior. These modes display distinct spatial and temporal profiles across various states of consciousness and cognitive conditions, as demonstrated using diverse electrophysiological and neuroimaging datasets.

First, by applying RPA to EEG data across graded levels of consciousness during general anesthesia,[29] we show that these sub-second anterior-posterior directional modes and their switching dynamics are most prominent during wakefulness and progressively diminish as consciousness fades, suggesting a disruption of organized information flow (Video S1).

Second, using simultaneous EEG-fMRI data,[30] we examined the functional relevance of these phase dynamics. The anterior-to-posterior mode correlated with higher-order networks, such as the default mode network (DMN) and the frontoparietal network (FPN), whereas the posterior-to-anterior mode was linked to the visual network (VN) and the dorsal attention network (DAN). These findings support the interpretation of anterior-to-posterior flow as top-down and posterior-to-anterior flow as bottom-up, linking EEG phase dynamics to network-level BOLD activity.

Third, using RPA, we assessed group-level differences of the mode-transition dynamics during resting state by comparing typically developing participants with an inattentive-type attention-deficit/hyperactivity disorder (ADHD) cohort, revealing reduced top-down and increased bottom-up activity in the ADHD group. Our findings support the theory that ADHD-inattentive symptoms are associated with decreased top-down control, leading to the lack of inhibition of bottom-up processes.[31] RPA also outperforms the traditional theta/beta power ratio (TBR) as a diagnostic marker.

Finally, using a coupled-oscillator model on a structural connectome,[32,33] we simulated dynamic phase relationships and demonstrated that distinct directional modes—and their transitions—emerge spontaneously from interactions among neural masses across the brain network. These results align with prior findings on traveling waves potentially arising from the brain's structural topology.[34,35] Our results also resonate with prior work showing that phase-lead/lag relationships alternate in large-scale networks with critical coupling strength,[26] and further show that these dynamics appear as alternating top-down and bottom-up directionality.

Collectively, our study introduces a comprehensive, real-time framework for understanding whole-brain dynamics, providing new insights into hierarchical processing, brain-state transitions, and neuropsychiatric conditions. We reveal that the fluctuating interplay between top-down and bottom-up processing is an intrinsic feature of large-scale brain dynamics and a fundamental mechanism underlying human information processing. By applying RPA, we uncover how levels of consciousness, external stimuli, and pathological conditions influence this delicate balance, paving the way for a deeper exploration of the fundamental mechanisms governing perception, cognition, and consciousness.

RESULTS

Defining RPA and comparison with other measures

Throughout this study, we focus on the alpha band (8–12 Hz), where transition dynamics are most prominent. However, similar patterns are observed in other bands as well—lower beta (12–20 Hz), theta (4–8 Hz), higher beta (20–30 Hz), delta (1–4 Hz), and gamma (30–50 Hz)—albeit with a progressively reduced prominence (analyses of other frequency bands are discussed in a subsequent section).

We first validate relative phase as a measure of directionality by comparing it to established metrics, including phase-lag

(B) Relative phases are spatially extrapolated to form a topographic map at each time point.
(C) Concatenating maps across time creates a topographic movie; *K*-means clustering identifies dominant patterns, and linear regression with these centroids as regressors yields time-varying coefficients $\hat{y}(t) = \beta_1(t) \cdot X_1 + \beta_2(t) \cdot X_2 + \varepsilon(t)$, where X_1 and X_2 are the first two dominant patterns.
(D) Relative phase (time-window averaged) is compared with dwPLI, traveling wave metrics, and EEG amplitude for frontal and parietal channel groups.
See also Figures S1, S2, and S3, Table S1, and Video S1.

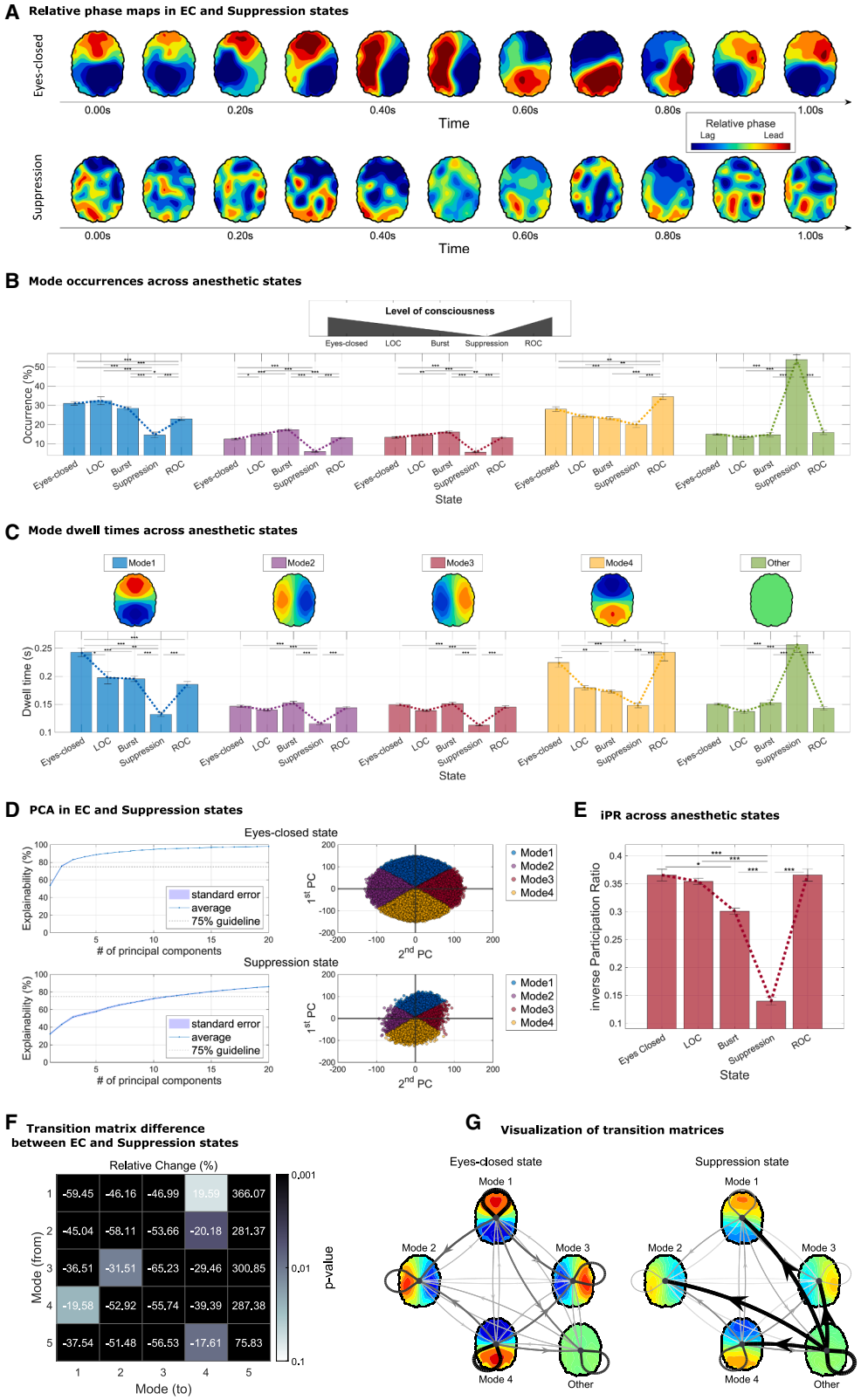

Figure 2. Statistics of relative phase dynamics in the general anesthesia dataset

(A) Mode probability density functions vary with level of consciousness; modes 1 and 4 are most closely tied to consciousness depth.

(B) Mode occurrence rates across anesthetic states.

(legend continued on next page)

indices and traveling-wave analyses. For validation, we applied RPA to eyes-closed resting-state EEG from the University of Michigan general anesthesia dataset,[29,36] recorded with 128 channels (experimental model and study participant details in the STAR Methods).

The framework for RPA is shown in Figure 1 (method details in the STAR Methods). Brain signals from each EEG channel were first decomposed into amplitude and phase components at each time point using the Hilbert transform, with the phase representing the precise timing of the signal within its periodic cycle. For each time point, we computed the relative phase for each channel by subtracting the global mean phase averaged across all channels. The resulting relative phase value for each channel j ranges continuously from -1 to $+1$ at each time point (Figures 1A and 1B; method details in the STAR Methods). A positive relative phase indicates that the signal from electrode j leads the global mean phase, whereas a negative value indicates that it lags behind. We hypothesize that these phase-lead/lag relationships serve as indicators of the directionality of information flow across the brain.[5,9–13,26] An example relative phase map is shown in Figure 1C. Additional examples from all datasets are provided in Figure S1A. After computing the relative phase maps, we characterized their patterns using K-means clustering and complementary linear regression scoring with the resulting K-means centroids.

For method comparison, the data were segmented into 2-s windows. Within each window, we computed amplitude from the Hilbert envelope, directional weighted phase-lag index (dwPLI) averaged over frontal/parietal electrode groups, and traveling-wave metrics using phase gradients. Directional phase-lag index (dPLI) and dwPLI quantify phase-lead/lag tendencies, with dwPLI reducing near-zero-lag effects related to volume conduction and noise.[25] The phase-gradient method estimates propagation from local phase gradients.[9,11,12]

Relative phase was computed per channel and averaged across regions and windows (method details in the STAR Methods). Relative phase correlated strongly with established measures (Figure 1D). In the frontal region, it exhibited $r = 0.887$ with dwPLI and $r = 0.817$ with frontal-to-posterior traveling waves. In the parietal region, correlations were $r = 0.892$ with dwPLI and $r = -0.813$ with front-to-back (FB) traveling waves utilizing the phase-gradient method ($p < 0.001$ for all). In contrast, relative phase, traveling-wave, and phase-lag measures yielded either no statistically significant correlations or only low correlations with signal amplitudes ($\rho \leq 0.304$), indicating that amplitude and phase dynamics contain distinct information[37] (Figure S1D).

Further comparisons confirmed consistent temporal correspondence between RPA and conventional traveling-wave measures across datasets (Figure S1C; Table S1). With all datasets combined, the RPA and the phase-gradient traveling-wave measure were strongly correlated ($r = 0.790$, $p < 0.001$; Figure S1C, left). This correspondence was also observed within individual datasets and conditions, with consistently high correlations ($\rho_1 \geq 0.660$, $p < 0.01$). Time-lagged cross-correlation analysis of the continuous signals showed peaks at the zero lag, indicating temporally aligned directional fluctuations. After transforming both signals into discrete directionality-switching event time series, the transition-based cross-correlations also peaked at zero lag ($\rho_2 \geq 0.446$, $p < 0.01$), suggesting that the two approaches capture similar switching dynamics (Figure S1C, right; Table S1).

We extended RPA into a real-time, whole-brain framework that overcomes the spatial and temporal constraints of prior methods, allowing for comprehensive analysis of real-time dynamics across the full scalp without requiring time-window averaging or specific channel selection.

RPA across diverse levels of consciousness

We next examined relative phase dynamics using the general anesthesia dataset[29,36] to assess their relationship with consciousness. As each participant underwent general anesthesia, they progressively transitioned through distinct states: eyes-closed resting state, loss of consciousness (LOC), burst period, suppression period, and recovery of consciousness (ROC). LOC and ROC were determined by responses to verbal commands. Burst and suppression periods marked the deepest unconscious states, characterized by alternating bursting and suppressed brain activities. For each state, we derived time-resolved relative phase topographic maps by computing them at each frame and subsequently aggregating across time (Figures 1B and 1C; Video S2). Clear transitions emerged: during the eyes-closed resting state, clear FB and back-to-front (BF) patterns appeared consistently, whereas in the suppression state, patterns were disorganized and unstable (Figure 2A; Video S2). Similar transition patterns were observed across all datasets, as illustrated by the examples in Figure S1A.

To quantify these dynamics, we applied K-means clustering to identify four dominant topographic modes (Figure 1C): FB and BF (anterior brain area phase leading posterior area and vice-versa), and left-to-right and right-to-left (left hemisphere phase leading right hemisphere and vice-versa). In analyzing occupancy rates and dwell times for each state, we can perform multiple linear regression using these identified dominant patterns as regressors (method details in the STAR Methods). Such a regression classifies the relative phase map at each time point by dominant mode, and the regression coefficients $\beta_1(t)$ and $\beta_2(t)$ determine whether each map matched a front-back or left-right pattern; if $|\beta_1(t)| > |\beta_2(t)|$, the map is classified as FB ($\beta_1(t) > 0$) or BF

(C) Mode dwell times across anesthetic states.
(D) PCA explainability: in the eyes-closed state, the first three PCs account for >70% of total variance; in suppression, ≥ 20 PCs are required to reach that threshold.
(E) The inverse participation ratio (iPR) decreases with deeper unconsciousness.
(F) Relative change (%) of the transition matrix between eyes-closed and suppression states (normalized to the eyes-closed mean). Cell colors indicate p values as shown in the colorbar.
(G) Transition matrices visualized as networks. Asterisks denote statistical significance: * $p < 0.05$, ** $p < 0.01$, *** $p < 0.001$. Error bars in the figures indicate standard error.
See also Figures S3 and S4, Table S2, and Video S2.

($\beta_1(t) < 0$); if $|\beta_1(t)| < |\beta_2(t)|$, it was classified as left-to-right ($\beta_2(t) > 0$) or right-to-left ($\beta_2(t) < 0$). Studying the regression coefficients is analogous to examining the principal-component analysis (PCA) loading scores in a time-ordered, frame-by-frame manner, with the additional advantage that the linear regression framework allows us to quantify variance not explained by the regressors through the residual term $\varepsilon(t)$.

We also note that this regression approach yields results that are approximately equivalent to 4-means clustering and PCA applied to the relative phase maps across time, consistent with the known relationship between *K*-means clustering and PCA, where principal components (PCs) approximately correspond to the centroids identified by *K*-means clustering (method details in the STAR Methods).

During the resting state, FB (mode 1) and BF (mode 4) modes dominated, with higher occupancy rates and longer dwell times in the order of 200 ms. In contrast, left-right modes (modes 2 and 3) were more transient. Across states of consciousness, FB and BF occupancy rates and dwell times systematically declined with LOC, and recovered toward the resting-state levels during ROC (Figures 2B and 2C). Statistically significant state-pair differences are indicated (all significant comparisons: $p < 0.05$). Using the residual $|\varepsilon(t)|$, we defined a fifth category, "Other," for maps that were poorly captured by the four centroids, labeling time points whose residual exceeded the 85th percentile of resting-state residuals. During suppression, the Other category became most prominent, while all four canonical modes (modes 1–4) were significantly reduced. The occupancy rates and dwell times for each mode are summarized in Table S2.

State differences were also distinguishable in the PCA structure. In the unconscious state, more PCs were required to explain the data, whereas in the resting state, the first two PCs (corresponding to four modes) explained 75% of the variance (Figure 2D). The inverse participation ratio (iPR)—which reflects the inverse of number of PCs required to explain the given data—decreased as consciousness diminished: from 36.59% (resting) to 35.45% (LOC), 30.07% (burst), and 13.95% (suppression), then returned to 36.61% during ROC (Figure 2E), indicating that relative phase patterns became increasingly disordered during unconsciousness (method details in the STAR Methods). Significant iPR differences were observed across states ($p < 0.05$ for resting and burst, resting and suppression, LOC and suppression, burst and suppression, and suppression and ROC).

The transition patterns also differed between conscious and unconscious states (Figures 2F and 2G). Transition rates into the Other mode were significantly higher in the suppression state, indicating greater randomness in brain wave patterns. In contrast, transitions among canonical modes 1–4 were generally reduced in the suppression state. Altogether, these findings highlight FB and BF phase dynamics as robust indicators of conscious state. We additionally performed a bootstrap analysis of the results summarized in Figure 2 to account for the limited sample size, and the results were qualitatively consistent with the original findings.

Analysis of the dominant mode dynamics across frequencies

We first examined whether the four canonical modes identified in the alpha band were also expressed in other frequency bands. Similar mode patterns were observed in lower beta (12–20 Hz), theta (4–8 Hz), higher beta (20–30 Hz), delta (1–4 Hz), and gamma (30–50 Hz), with prominence decreasing in that order relative to the alpha band (Figures S2B and S2C).

We next asked whether these patterns, and the transitions between them, reflect a single broadband phenomenon or distinct band-specific structure. For each frequency band, we computed pairwise correlations of mode-transition time series across bands (statistical analysis and computational model in the STAR Methods): (1) non-adjacent frequency bands exhibited low correlations, indicating genuine frequency-specific structure and (2) neighboring bands showed only moderate similarity (Figure S2D). These cross-band correlations were strongest at rest and substantially reduced under general anesthesia. Together, these results argue against a single broadband dynamic process and instead show that each band exhibits partially distinct dynamics while preserving the same dominant spatial mode classes, for which patterns were highly similar across frequency bands (mode-pattern correlations > 0.98).

RPA of simultaneous EEG-fMRI during resting and stimulus states

To assess the functional relevance of FB and BF phase modes, we analyzed simultaneous EEG-fMRI data collected during alternating blocks of eyes-closed rest and a 12 Hz flashing checkerboard task,[30] which robustly activates the visual network (VN). Differences in BOLD activity between the rest and stimulation conditions are shown in Figure 3A, revealing that higher-order cognitive regions were more active during rest, whereas visual sensory areas showed greater activation during stimulation (method details in the STAR Methods).

Relative phase topographic maps, averaged across trials and participants, revealed frontal phase-leading patterns during rest and parietal-leading patterns during stimulation (Figure 3A, right). From a time-series analysis perspective, the long-term trend persisting after averaging across trials and participants revealed a systematic bias toward either the FB or the BF mode, depending on the brain state.

To more comprehensively characterize the relationship between EEG relative phase patterns, dynamics, and fMRI BOLD signals, we examined activation across 17 canonical functional networks using established parcellations.[38] The FB mode expression—quantified by the regression coefficient $\beta_1(t)$—was positively correlated with DMN activity (DMA, DMB, and DMC; $r > 0.5$, $p < 0.001$), whereas the BF mode expression ($-\beta_1$) was associated with visual central (VC) network activity ($r = 0.58$, $p < 0.001$) (Figures 3B and 3C). We further mapped whole-brain correlations between β_1 and BOLD signals using the 1,000-parcel Schaefer atlas. FB mode expression correlated significantly not only with DMN but also with other higher-order networks, including the frontoparietal network (FPN: especially FPB and FPC) and temporal-parietal (TP) network ($p < 0.001$; Figures 3C and 3D).

Together, these findings suggest that FB phase dynamics reflect top-down processing via anterior-to-posterior flow, aligned with internally guided cognitive states, whereas BF dynamics reflect bottom-up processing aligned with externally driven sensory input. Based on these results, we define the FB pattern as the top-down mode, representing information flow

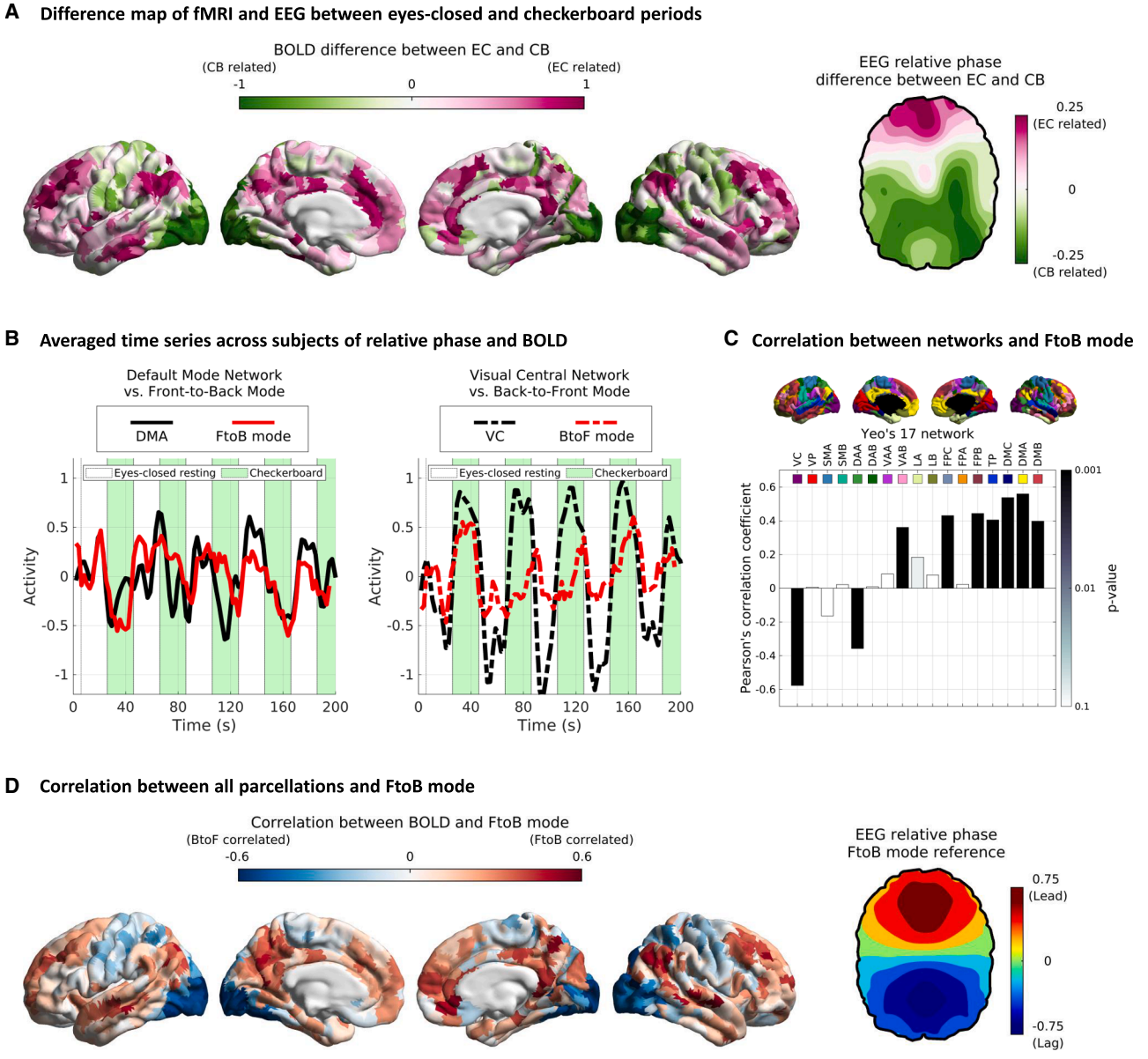

Figure 3. Brain network correspondence of relative phase patterns using simultaneous EEG-fMRI recordings

To investigate the functional relevance of front-to-back (FB) and back-to-front (BF) modes, RPA patterns were compared with BOLD activity during eyes-closed rest (EC) and a 12 Hz flashing checkerboard task (CB).

(A) Left: EC − CB BOLD difference maps. Right: EC−CB EEG difference map. Purple: EC > CB; green: CB > EC.

(B) Time series of β_1 (FB mode) and default mode A (DMA) BOLD activity (left), and $-\beta_1$ (BF mode) and visual central (VC) BOLD activity (right).

(C) Pearson's *r* between β_1 and all 17 Yeo networks. Bar colors indicate *p* values as shown in the colorbar.

(D) Left: whole-brain β_1 versus BOLD correlation map using the Schaefer 1,000-parcel atlas. Red indicates FB-correlated regions, and blue indicates BF-correlated regions. Right: reference map of the EEG relative phase FtoB mode (mode 1) used for the correlation shown on the left. Red indicates phase-leading regions, and blue indicates phase-lagging regions.

from higher-order cognitive anterior regions to posterior regions, and the BF pattern as the bottom-up mode, representing information flow in the opposite direction.

RPA in control and ADHD groups

To evaluate the cognitive relevance of dominant phase modes, we applied RPA to resting-state EEG from ADHD-inattentive and control groups. Among multiple neuroscientific approaches to understanding ADHD symptoms, ranging from neurotransmitter-level theories to network- and cognitive-level models,[14,39–41] cognitive-level theories suggest the ADHD group exhibits reduced top-down signaling and impaired coordination between top-down and bottom-up processes,[31,42,43] an imbalance believed to contribute especially to the inattentive symptoms. Given RPA's sensitivity to these dynamics, we tested whether phase mode patterns reflect attentional deficits associated with ADHD.

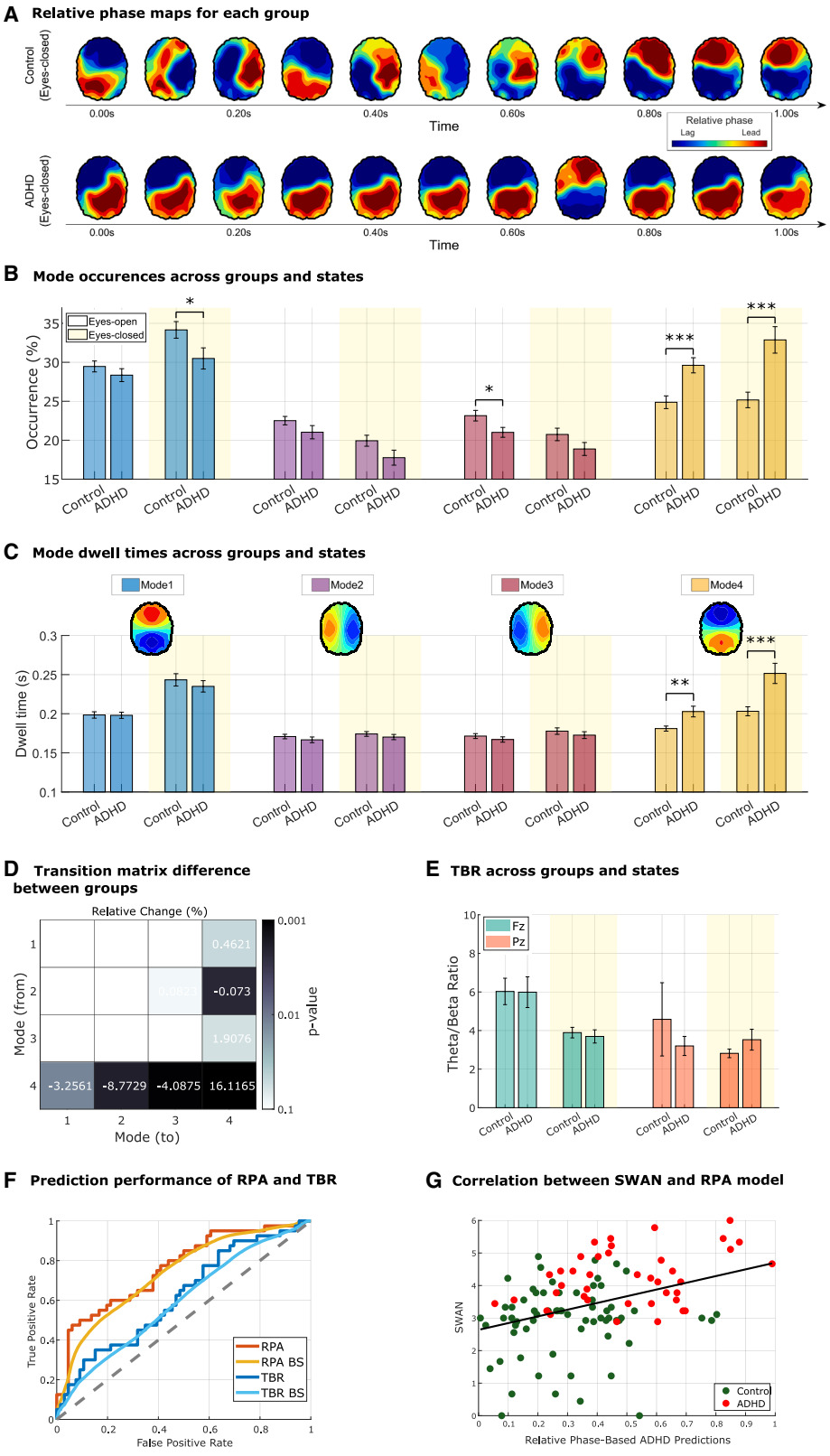

Figure 4. RPA applied to the HBN ADHD-inattentive dataset

(A) Representative eyes-closed relative phase snapshots for control and ADHD-inattentive participants; ADHD-inattentive participants dwell more in the back-to-front mode.

(legend continued on next page)

We analyzed eyes-open and eyes-closed EEG from the Healthy Brain Network (HBN) dataset.[44] In the eyes-closed condition, control participants showed dynamic mode switching every ~200 ms, whereas ADHD participants remained longer in the BF (mode 4) pattern (Figures 4A and S5). Quantitatively, the ADHD group exhibited significantly higher mode 4 occupancy and dwell time—by 30.6% and 23.9%, respectively—relative to controls ($p < 0.001$, false discovery rate [FDR]-corrected; Figures 4B and 4C). They also showed reduced expression of FB (mode 1) patterns ($p < 0.05$), suggesting deficient top-down signaling. The ADHD group also showed reduced expression of transient modes, with the decrease in mode 3 occurrence in the eyes-open state reaching statistical significance. Because modes 2 and 3 correspond to transient lateral patterns that often bridge anterior-posterior modes, this reduction may indicate decreased lateral transitional dynamics. Thus, the increased mode 4 dominance may reflect a broader reorganization of mode occupancy, characterized primarily by enhanced bottom-up dominance, reduced top-down expression, and reduced expression of transitional modes. Transition analysis further showed that ADHD participants had elevated mode 4-to-mode 4 self-transitions ($p < 0.001$) and decreased transitions from mode 4 to other modes ($p < 0.01$), supporting the hypothesis of slower, bottom-up-biased dynamics in ADHD (Figure 4D, bottom row of the matrix). The occupancy rates and dwell times for each mode are summarized in Table S2.

We then compared RPA with the conventional TBR, used in the Neuropsychiatric EEG-Based ADHD Assessment Aid (NEBA), the first Food and Drug Administration (FDA)-approved EEG assessment aid for ADHD. Consistent with prior reports,[45,46] it did not differ significantly between the inattentive and control groups (Figure 4E). Receiver operating characteristic curve analysis showed that the logistic model-based RPA outperformed the TBR model in individual-level diagnostic prediction (Figure 4F; statistical analysis and computational model in the STAR Methods). The RPA model achieved a performance score of 0.76 (0.73 bootstrap-validated), versus 0.62 (0.59 bootstrap-validated). We also found a significant correlation between the RPA model's diagnostic score and the Strengths and Weaknesses of ADHD Symptoms and Normal Behavior Scale (SWAN) inattentive score[47] ($r = 0.38$, $p < 0.001$; Figure 4G), indicating meaningful alignment between RPA and behavioral measures. While SWAN helps reduce false negatives, RPA may reduce false positives. Notably, distinguishing between control and ADHD subjects in the upper-left quadrant of the diagnostic scatter may offer valuable insights, warranting further investigation.

Together, these results support the theory that ADHD-inattentive symptoms reflect impaired top-down signaling and imbalanced top-down/bottom-up coordination. Additionally, RPA demonstrates greater potential as a biomarker for the ADHD-inattentive subtype.

Simulating relative phase dynamics via a coupled-oscillator model

To investigate the mechanism underlying mode fluctuations, we simulated relative phase dynamics using a Kuramoto model whose connectivity patterns are specified by a human structural connectome (statistical analysis and computational model in STAR Methods).[48] We hypothesized that stochastic fluctuations in the coupling parameter c_0, modeled as an Ornstein-Uhlenbeck (OU) process, could reproduce the empirical FB and BF transition dynamics (Figure S6).

High-degree nodes phase lagged during mode 1 (top-down) and phase led during mode 4 (bottom-up) (Figure S6A). These corresponded to significant correlations between anterior-posterior coordinates and relative phase values averaged along the anterior-posterior axis: $r = -0.249$ ($p = 0.00752$) for mode 1, and $r = 0.255$ ($p = 0.00608$) for mode 4 (Figure S6A). The model reproduced key features of the temporal dynamics of the empirical data (Figure 5C): greater occupancy and longer dwell times for modes 1 and 4, minimal transitions between modes 2 and 3, and transition matrices showed diagonal dominance reflecting a tendency to remain in the same mode, with modes 2 and 3 primarily mediating transitions between modes 1 and 4 (Figures 5C and 5D).

These results demonstrate that a simple coupled-oscillator model with stochastic modulation can replicate the spatial and temporal structure of observed phase dynamics. These structures emerge as a consequence of structural constraints imposed on the model oscillators, which introduce hierarchical organization in terms of their degrees (number of connections). Alternative processes with multiple stable states also replicated empirical patterns (Figure S6B), suggesting that top-down and bottom-up modes may correspond to attractor states in brain network dynamics.

DISCUSSION

What are the dominant modes of directionality at the whole-brain level? What are the real-time transition dynamics between these modes? We addressed these questions by establishing relative phase as a robust, versatile, and clinically relevant measure of brain dynamics. Leveraging RPA, we found that (1) the anterior-to-posterior (top-down) versus posterior-to-anterior (bottom-up) directional patterns are fundamental modes of human brain dynamics, with the brain rapidly fluctuating between these two states on a sub-second scale; (2) these dynamic properties are most pronounced during full consciousness and diminish as

(B) Mode probability density functions across eyes-open and eyes-closed conditions.
(C) Mode dwell time distributions.
(D) Relative difference matrix between group transition matrices during eyes-closed rest, normalized by the control group mean. Cell colors indicate p values as shown in the color bar.
(E) Theta/beta ratios at Fz and Pz electrodes for both groups.
(F) Receiver operating characteristic curves comparing RPA and TBR for individual-level diagnostic prediction.
(G) Correlation between SWAN inattentive scores and RPA diagnostic values.
Asterisks indicate statistical significance: $^*p \leq 0.05$, $^{**}p \leq 0.01$, $^{***}p \leq 0.001$. Error bars in the figures indicate standard error.
See also Figure S5 and Table S2 and Video S3.

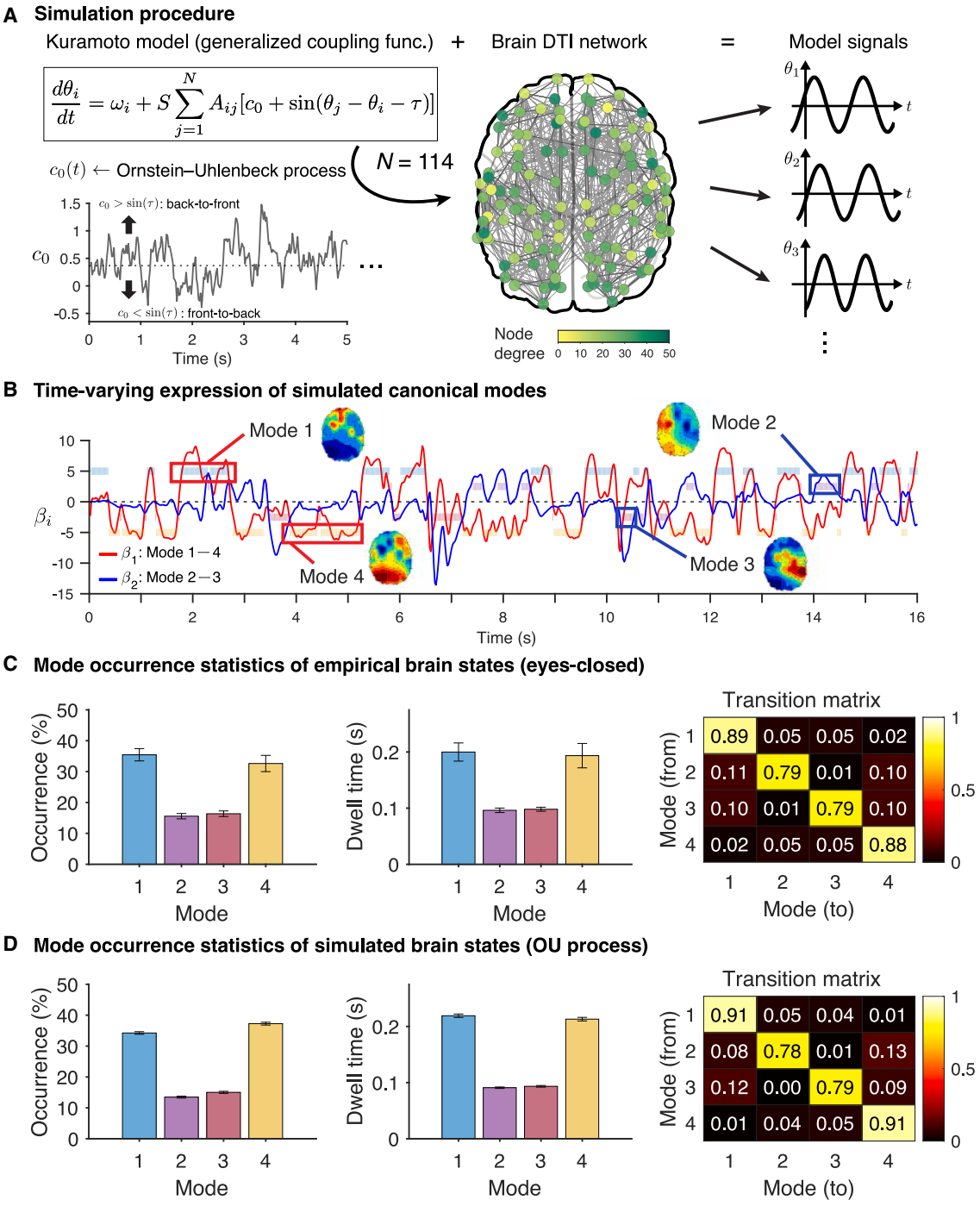

Figure 5. Simulation of relative phase dynamics using the Kuramoto coupled-oscillator model

(A) Simulation schematic: Kuramoto model with generalized coupling on the Lausanne 114-node structural network; c_0 evolves via an Ornstein-Uhlenbeck process (dotted lines: fixed point $c_0 = \sin(\tau)$).

(B) Simulated relative phase topographic map snapshot.

(C) Empirical mode statistics from University of Michigan (UofM) eyes-closed data: occurrence distribution, dwell times, and transition matrix; error bars = SEM across subjects.

(D) Same statistics for simulated data averaged over 50 initial conditions; parameters: $S = 1.8$, $\tau = 0.12\pi$, $\psi = 6$, $\sigma = 1.5$.

See also Figure S6.

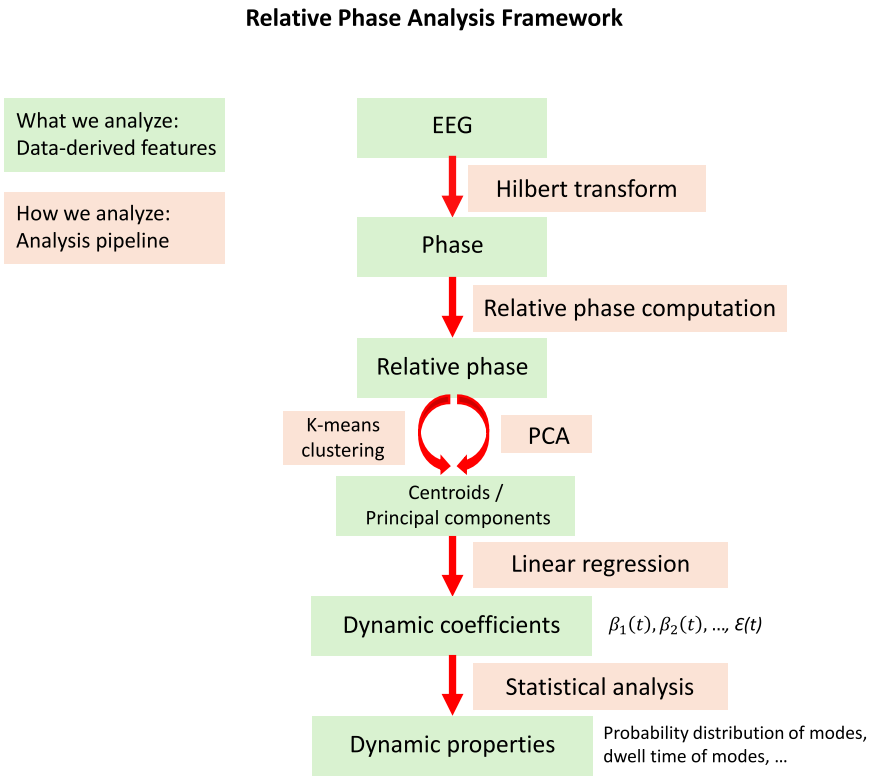

Figure 6. Schematic of the RPA framework

The RPA pipeline: (1) Hilbert transform to extract instantaneous phase; (2) compute relative phase maps across time; (3) *K*-means clustering or PCA to identify dominant spatial patterns; (4) linear regression with centroids/PCs as regressors, yielding $\beta_1(t), \beta_2(t), \varepsilon(t)$; and (5) statistical analysis of coefficient time series (mode probability distributions and dwell times). Green boxes: data-derived features; pink boxes: analytical procedures.

consciousness fades; (3) the directional modes are associated with the BOLD activity of corresponding functional networks (anterior-to-posterior mode with DMN and FPN, posterior-to-anterior mode with VN); (4) developing individuals and those with the ADHD-inattentive subtype exhibit group-level differences in their relative phase profiles and dynamics; and (5) a generalized coupled-oscillator brain network model reproduces the observed mode-transition dynamics.

RPA reveals real-time, whole-brain dynamics of sub-second anterior-posterior directionality transitions

RPA provides a real-time framework for quantifying phase dynamics, enhancing our ability to investigate large-scale neural interactions beyond previous methods. Unlike time-window-based phase-lag measures or region-specific traveling-wave analyses, RPA—the complete pipeline of which is schematized in Figure 6—offers continuous tracking of neural phase relationships across the whole cerebral cortex. A more recent traveling-wave analysis has also characterized large-scale phase dynamics without strict regional preselection.[49] However, traveling-wave analyses generally rely on spatial or spatiotemporal derivatives of the phase field, which are more sensitive to noise and often require smoothing or regularization.[50,51] By contrast, RPA operates directly on phase relationships, yielding a compact and potentially more stable real-time representation of whole-brain directionality dynamics. Additionally, RPA holds promise for neurofeedback applications, where the ability to monitor real-time neural dynamics is crucial.

Leveraging RPA, we identified sub-second transitions between dominant top-down and bottom-up directional modes. Prior studies suggest that such fluctuations, or more generally, the alternation between internally and externally biased processing states, occur across multiple spatial and temporal scales.[18] Internally biased processing denotes states dominated by higher-order, memory-based, or predictive processes (e.g., DMN/FPC), whereas externally biased processing denotes states dominated by sensory- or stimulus-driven processes (e.g., DAN/VN). These dynamics span multiple scales from microcircuit interactions (tens of ms) to EEG/MEG wave dynamics (hundreds of ms) and fMRI network transitions (seconds), and reflect a continuous shifting balance rather than a strict binary alternation. This oscillatory balance has also been proposed as a fundamental signature of human brain information processing across multiple levels of organization.[18]

Importantly, the "modes" identified by RPA should be interpreted as macroscopic processing biases rather than uniform, all-or-none configurations across circuits and subregions. Feedforward and feedback interactions may coexist, while large-scale EEG phase structure reflects a momentary bias in their relative dominance, manifesting as a coarse anterior-posterior directional tendency. This interpretation is consistent with network-level accounts of internally versus externally biased processing[18] and with electrophysiological traveling-wave studies showing state-dependent propagation biases during perception and cognition.[10–12] Relatedly, the identification of four dominant phase topographies does not imply that brain information processing is limited to four discrete regimes. Rather, these modes reflect a low-dimensional organization of macroscopic phase dynamics, in which a continuous distribution of patterns is well captured by a small number of dominant axes. In our analysis, the first two PCs—corresponding to the four dominant phase modes—account for most of the variance, providing a compact summary of an underlying continuous dynamical structure.

Event-related potential (ERP) studies from EEG and ECoG indicate that responses to external stimuli unfold within sub-second timescales, consistent with our finding that whole-brain bottom-up versus top-down switching occurs approximately every 200 ms. This timescale falls within the range of rhythmic attentional sampling and perceptual cycles reviewed in VanRullen,[27]

where behavioral periodicities are commonly reported at ~ 3–12 Hz, corresponding to cycle durations of approximately 83–333 ms. Thus, the observed switching occurs within a temporal regime previously associated with rhythmic sampling of perception and attention. The timescale also aligns with MEG studies showing that large-scale electrophysiological network states can be transiently expressed over ~100–200 ms,[28] as well as recurrent predictive-processing update cycles proposed to operate on sub-second intervals.[18] RPA may therefore capture a directional component of these rapid network-state reconfigurations, tracking not only which large-scale pattern is active, but whether the dominant phase bias is anterior-to-posterior or posterior-to-anterior. At this timescale, rapid switching between directional biases may support flexible integration of feedforward and feedback information, enabling continuous updating of internal models[18,52]: the observed alternation between top-down and bottom-up biases may reflect an intrinsic temporal regime for coordinating internal predictions with incoming sensory input.

Crucially, we observed that these fluctuations are not solely stimulus-driven but also emerge spontaneously during resting states, suggesting an intrinsic top-down versus bottom-up modulation independent of external input. This finding highlights a fundamental, self-organizing mechanism of cortical dynamics. Additionally, we observed that both top-down and bottom-up directionalities extend across all frequency bands up to 50 Hz, suggesting that the macroscopic phase organization captured by RPA is a pervasive feature of cortical dynamics rather than a band-specific artifact.

This does not imply identical functional roles across frequencies or contradict predictive-coding accounts of lower-frequency feedback and higher-frequency feedforward signaling. Instead, similar macroscopic directionality classes are detectable across bands, while their temporal dynamics remain frequency-specific. Future work will examine how task demands reshape frequency-specific top-down and bottom-up processing.[10,53,54]

Sub-second anterior-posterior directionality transitions are linked to BOLD dynamics and distinguish diverse brain states

RPA offers a promising tool for assessing consciousness levels in clinical settings, where differentiating brain states under anesthesia remains a challenge. We used the anesthesia dataset to identify and validate dominant sub-second relative phase patterns because it provides high-quality continuous EEG with well-separated, graded consciousness levels (awake → light sedation → deep anesthesia → recovery), enabling a controlled test of state-dependent robustness. Traditional amplitude- and phase-based measures often fail to distinguish states such as burst and resting periods.[1,4] In contrast, RPA captures reductions in dominant directional modes that reliably track consciousness levels. Notably, the reduction prominently appears in both the alpha and low beta bands, and exploring how different anesthetic agents modulate these dynamics across frequency bands may offer insights into their neural mechanisms.

Simultaneous EEG-fMRI may provide an insightful link between electrophysiological directionality and BOLD-based network transitions. By comparing resting and checkerboard tasks, we mapped FB and BF EEG phase dynamics onto top-down and bottom-up BOLD network activity. Future research will extend this analysis to EEG-fMRI data acquired with more nuanced and naturalistic stimuli, aiming to capture mode-transition dynamics in more natural settings. Applying RPA directly to BOLD time series may also reveal novel insights into the directional propagation of BOLD signals, and integrating RPA with established approaches could yield a more robust framework for inferring BOLD dynamics while addressing fMRI's inherent temporal limitations.

These results also complement and extend the EEG microstate literature, where associations between amplitude-defined topographies and BOLD networks have been studied primarily from an activity-based perspective.[55–61] In contrast, RPA provides a possible mechanistic bridge between electrocortical dynamics and BOLD network activity, offering a parsimonious decomposition of the dynamics into alternating top-down and bottom-up flows through the correspondence between FB versus BF directionality patterns and the activity of higher- versus lower-order areas.

RPA also distinguished individuals with inattentive-type ADHD from controls, revealing increased bottom-up and decreased top-down mode expression. These findings align with cognitive theories implicating reduced top-down inhibition in ADHD.[31,62] RPA may further bridge brain dynamics and behavior, offering a candidate EEG biomarker and mechanistic insight into attentional dysfunction. It may serve as a valuable tool for supporting integrative models that connect cognition, emotion, and environmental influences[41,63,64] and for tracking intervention outcomes through changes in directional phase dynamics.

Computational modeling of sub-second directionality modulation provides predictive insights

Our computational modeling suggests that the FB and BF directionality modes and the transitions between them can spontaneously emerge from the underlying structural network of the brain. These findings build upon prior modeling results of phase-lead/lag alternations in networks,[26] and align with previous findings suggesting that traveling waves can naturally arise from cortical topology.[34,35]

In the top-down (FB) mode, sparsely connected regions, particularly in the prefrontal cortex, tend to phase lead, establishing a front-leading-back pattern of information flow. This reflects the structural characteristics of prefrontal areas, which are relatively sparse in local connectivity. In contrast, occipital regions are more densely interconnected and play a central role in shaping the bottom-up (BF) mode, where densely connected areas lead the phase dynamics. Notably, despite their local sparsity, prefrontal regions function as long-range connector hubs, integrating information across distinct cortical modules.[65] Our simulation results and interpretations align with previous findings that prefrontal regions exhibit lower connection density yet higher participation in large-scale, integrative communication—highlighting their role in coordinating distributed brain networks.[65,66] As such, our simulation framework suggests that hierarchical cortical structure may be the crucial feature underlying RPA-like dynamics.

Introducing a stochastic coupling term (c_0) caused the dominant modes to function as attractor states. In our

coupled-oscillator framework, c_0 serves as an intermediary between direct and diffusive coupling,[67,68] corresponding in biological terms to electrical and chemical synaptic coupling, respectively.[69,70]

Higher c_0 values (associated with bottom-up mode) reflect dominance of electrical synapses via gap junctions. Lower c_0 values (top-down mode) correspond to chemical synapses where action potentials propagate via neurotransmitters. Our model thus predicts that transitions between directional modes may reflect shifts in the balance between these two coupling mechanisms, which remain to be investigated empirically. Another possible interpretation of our model is that the c_0 term reflects the relative dominance of external stimuli in the network: when c0 exceeds $\sin(\tau)$, external stimuli are more influential on network dynamics (bottom-up mode); when c_0 is smaller than $\sin(\tau)$, intrinsic network dynamics dominate (top-down mode). Our framework extends the previous theoretical proposals on the functional implications of having two co-existing forms of coupling in the oscillator system.[67–69,71,72]

Limitations and future perspectives

Analytically, phase lead-lag alone does not establish microcircuit-level causality. Here, we use "directionality" to denote a macroscopic bias arising from oscillatory signals in an interacting functional network: consistent phase leading indicates that one signal tends to precede and directly or indirectly influence another, and can therefore serve as a practical proxy for directional propagation. This interpretation is supported by previous coupled-oscillator modeling showing agreement between phase-lead/lag metrics and windowed causality measures, such as Granger causality and transfer entropy.[7] In this study, simultaneous EEG-fMRI provides convergent network-level support, with top-down dominance co-occurring with DMN/FPC activation and bottom-up dominance aligning with DAN/VN activation.

We also acknowledge the ongoing debate on whether macroscopic traveling waves are genuine physiological wave packets versus epiphenomenal manifestations of coordinated phase gradients.[73,74] RPA does not require a strong "wave packet" interpretation; it detects dominant global phase patterns with sub-second resolution. The strong dissociations across consciousness, the ADHD versus control effects, and the EEG-fMRI network correspondence argue for physiological relevance even with the epiphenomenal interpretation.

We conclude by noting several limitations.

(1) Relative phase dynamics showed only weak correlation with amplitude dynamics, suggesting that amplitude and phase each capture complementary yet distinct aspects of brain dynamics.[37] Future studies with more detailed analyses (e.g., comparisons of relative phase dynamics and EEG microstates) may uncover richer phase-amplitude relationships and provide deeper interpretations, particularly in relation to BOLD network activity.

(2) RPA can also be applied to source-reconstructed signals, but such extensions should be interpreted cautiously, given inverse-problem ambiguity and spatial leakage; developing leakage-aware source-level implementations and validations is a promising future direction.

(3) Transitions between anterior-posterior and lateral (left-right) gradients may appear as rotating or spiral-like organization of the global phase field at appropriate timescales, reminiscent of prior spiral-wave observations[75,76]; a direct comparison with spiral-wave phenomena would be an important direction for future studies using high-density EEG/MEG or ECoG.

(4) The left-right and right-left phase patterns: these modes appeared transiently, often serving as bridges between dominant frontoparietal modes rather than sustained processing regimes. Such lateralized modes may reflect asymmetries in sensory input, attentional allocation, or network-level coordination and also relate to known hemispheric specialization. More generally, the number and nature of dominant phase patterns identified by RPA may vary across tasks and stimuli.

(5) Our analyses focused on resting-state data and a strong visual stimulus. Extending RPA to task-based paradigms will be essential for relating directional modes to cognitive functions such as attention and memory. For example, alpha phase lags in posterior regions during working memory distraction[77] may reflect increased top-down control (mode 1), consistent with our framework. Auditory paradigms (e.g., oddball paradigms[78–80]) may also yield distinct relative phase dynamics due to the temporal location of the auditory cortex.

(6) The relationship between relative phase modes and peripheral physiological signals (e.g., electrocardiogram, eye movements, and muscle activity) remains to be explored.

(7) While RPA is sensitive to changes in consciousness, its clinical value should be compared against established metrics such as the bispectral index (BIS) and patient state index (PSI).

(8) Broader validation of RPA across ADHD subtypes, comorbidities, and diverse age and sex groups is essential for generalization. This study focused on the inattentive subtype and adolescents ($\geq$ 11 years) to avoid developmental confounds in alpha rhythms.

(9) Our coupled-oscillator model could be refined using more biologically grounded frameworks, such as the Wilson-Cowan model, to probe biophysical mechanisms of mode transitions.

(10) Lastly, in David Marr's levels of analysis—computational, algorithmic, and implementational[81,82]—our model is at the implementation level. Only the expansion and combination of our model with the algorithmic and computational levels will provide a complete picture of how information is processed via the top-down and bottom-up switching with respect to the external world and internal model construction.

Conclusion

This study introduces RPA as a powerful and versatile tool for investigating the brain dynamics, offering new insights into

brain-state transitions, hierarchical processing, and neuropsychiatric conditions. Our findings demonstrate that the fluctuating interplay between top-down and bottom-up processing is an intrinsic property of large-scale brain dynamics, reinforcing a dynamical systems perspective in which the brain continuously reconfigures its information processing organization. Our study offers a new research avenue exploring how external stimuli, cognitive demands, and pathological conditions influence this delicate balance. By integrating RPA with experimental neuroscience, we can investigate how spontaneous directional fluctuations shape perception, cognition, and consciousness, ultimately advancing our understanding of the fundamental principles of neural computation.

RESOURCE AVAILABILITY

Lead contact

Requests for further information and resources should be directed to and will be fulfilled by the lead contact, Joon-Young Moon (joon.young.moon@gmail.com).

Materials availability

This study did not generate any new, unique reagents.

Data and code availability

- The EEG dataset for the general anesthesia presented in this article cannot be deposited in a public repository because the human volunteers did not consent to public access at the time of recruitment. Requests to access these datasets should be directed to the lead contact.
- The simultaneous EEG-fMRI analysis utilized a publicly available dataset, accessible at https://fcon_1000.projects.nitrc.org/indi/retro/nat_view.html.
- The ADHD versus typically developed EEG analysis utilized a publicly available dataset, accessible at https://fcon_1000.projects.nitrc.org/indi/cmi_healthy_brain_network/.
- All the code used for analyses and simulations reported in this paper are publicly available at https://github.com/youngjai/RelativePhaseAnalysis.[83]
- Pedagogical tutorial code for RPA are publicly available at https://github.com/onemoon4u/RelativePhaseAnalysis.[84]

ACKNOWLEDGMENTS

This work was supported by IBS-R015-Y3 (to J.-Y.M., Y.C., and Y.K.) from the Institute for Basic Science of Korea (IBS), by the Basic Science Research Program through the National Research Foundation of Korea (NRF) funded by the Ministry of Education of Korea (RS-2023-00272652; to Y.P.), by the National Research Foundation of Korea (NRF) grant funded by the Korea Government (MSIT) (NRF-2022R1C1C1007095, RS-2023-00217361, and RS-2024-00398768; to S.-J.H.), by the DeepTech TIPS funded by the Ministry of SMEs and Startups (RS-2023-00302377; to H.K.), and by the National Institutes of Mental Health of USA (R01-MH119099 to C.J.H. and R01-2P50MH109429 subawarded to C.J.H.). We thank Hae Seong Lee for his help in the numerical simulations. We thank Dongho Kim for his advice on the framework of the analysis. We thank Heonsoo Lee for his advice in analyzing the general anesthesia dataset. We thank Qawi K. Telesford for his advice in preprocessing and analyzing the simultaneous EEG-fMRI dataset. We thank Jong-eun Lee for his advice in analyzing the ADHD dataset. We thank Eunhee Ji for her advice and comments on fMRI analysis and results. We thank Sunhyun Min, Seoyeon Kim, Jehyeop Lee, Minseo Cho, Jiwon Kim, and F. D. Poohy for their support in carrying out the study.

AUTHOR CONTRIBUTIONS

Y.P., Y.C., H.K., and J.-Y.M. designed the study. Y.K., J.H.W., H.C., T.X., U.L., S.-J.H., and C.J.H. provided input and revisions. Y.P., H.K., and J.-Y.M. developed the pipeline of the relative phase analysis. Y.P., Y.C., H.K., Y.K., J.L., and J.-Y.M. developed and implemented the data analysis. J.H.W. and J.-Y.M. developed and conducted the numerical simulations. Y.C., Y.K., and H.C. performed the statistical analysis. G.A.M., T.X., U.L., and S.-J.H. provided datasets. Y.P., Y.C., Y.K., J.H.W., and J.-Y.M. wrote the manuscript, which was revised by H.K., J.L, H.C., U.L., S.-J.H., and C.J.H.

DECLARATION OF INTERESTS

The authors declare no competing interests.

STAR★METHODS

Detailed methods are provided in the online version of this paper and include the following:

- KEY RESOURCES TABLE
- EXPERIMENTAL MODEL AND STUDY PARTICIPANT DETAILS
  - General anesthesia EEG data (UofM: University of Michigan)
  - Resting vs. checkerboard task from simultaneous EEG-fMRI data (NKI: Nathan Kline Institute)
  - ADHD/Control EEG data (HBN: Healthy Brain Network)
- METHOD DETAILS
  - EEG state extraction for the UofM general anesthesia dataset
  - Preprocessing of the NKI fMRI dataset
  - Preprocessing of HBN EEG dataset
  - Relative Phase Analysis of EEG signals
  - Choosing the optimal temporal scale of RPA
  - *K*-means clustering of the relative phase patterns
  - Linear regression using the centroids as regressors
  - Principal Component Analysis (PCA) of relative phase dynamics
  - Statistics over brain states
  - Other Measures
  - Statistical Analysis and Computational Model

SUPPLEMENTAL INFORMATION

Supplemental information can be found online at https://doi.org/10.1016/j.cub.2026.06.014.

Received: September 26, 2025
Revised: March 24, 2026
Accepted: June 5, 2026
Published: July 2, 2026

REFERENCES

1. Lee, U., Kim, S., Noh, G.-J., Choi, B.-M., Hwang, E., and Mashour, G.A. (2009). The directionality and functional organization of frontoparietal connectivity during consciousness and anesthesia in humans. Conscious. Cogn. *18*, 1069–1078. https://doi.org/10.1016/j.concog.2009.04.004.
2. Rabinovich, M.I., Afraimovich, V.S., Bick, C., and Varona, P. (2012). Information flow dynamics in the brain. Phys. Life Rev. *9*, 51–73. https://doi.org/10.1016/j.plrev.2011.11.002.
3. Melloni, L., van Leeuwen, S., Alink, A., and Müller, N.G. (2012). Interaction between bottom-up saliency and top-down control: how saliency maps are created in the human brain. Cereb. Cortex *22*, 2943–2952. https://doi.org/10.1093/cercor/bhr384.
4. Lee, U., Ku, S., Noh, G., Baek, S., Choi, B., and Mashour, G.A. (2013). Disruption of frontal-parietal communication by ketamine, propofol, and sevoflurane. Anesthesiology *118*, 1264–1275. https://doi.org/10.1097/ALN.0b013e31829103f5.
5. Moon, J.-Y., Lee, U., Blain-Moraes, S., and Mashour, G.A. (2015). General relationship of global topology, local dynamics, and directionality in large-scale brain networks. PLOS Comput. Biol. *11*, e1004225. https://doi.org/10.1371/journal.pcbi.1004225.

6. Hillebrand, A., Tewarie, P., Van Dellen, E., Yu, M., Carbo, E.W., Douw, L., Gouw, A.A., Van Straaten, E.C., and Stam, C.J. (2016). Direction of information flow in large-scale resting-state networks is frequency-dependent. Proc. Natl. Acad. Sci. USA *113*, 3867–3872. https://doi.org/10.1073/pnas.1515657113.

7. Moon, J.-Y., Kim, J., Ko, T.-W., Kim, M., Iturria-Medina, Y., Choi, J.-H., Lee, J., Mashour, G.A., and Lee, U. (2017). Structure shapes dynamics and directionality in diverse brain networks: mathematical principles and empirical confirmation in three species. Sci. Rep. *7*, 46606. https://doi.org/10.1038/srep46606.

8. Muller, L., Chavane, F., Reynolds, J., and Sejnowski, T.J. (2018). Cortical travelling waves: mechanisms and computational principles. Nat. Rev. Neurosci. *19*, 255–268. https://doi.org/10.1038/nrn.2018.20.

9. Zhang, H., Watrous, A.J., Patel, A., and Jacobs, J. (2018). Theta and alpha oscillations are traveling waves in the human neocortex. Neuron *98*, 1269–1281.e4. https://doi.org/10.1016/j.neuron.2018.05.019.

10. Alamia, A., and VanRullen, R. (2019). Alpha oscillations and traveling waves: Signatures of predictive coding? PLoS Biol. *17*, e3000487. https://doi.org/10.1371/journal.pbio.3000487.

11. Alamia, A., Terral, L., D'Ambra, M.R., and VanRullen, R. (2023). Distinct roles of forward and backward alpha-band waves in spatial visual attention. eLife *12*, e85035. https://doi.org/10.7554/eLife.85035.

12. Mohan, U.R., Zhang, H., Ermentrout, B., and Jacobs, J. (2024). The direction of theta and alpha travelling waves modulates human memory processing. Nat. Hum. Behav. *8*, 1124–1135. https://doi.org/10.1038/s41562-024-01838-3.

13. Moon, J.-Y., Müsch, K., Schroeder, C.E., Valiante, T.A., and Honey, C.J. (2024). Inter-regional delays fluctuate in the human cerebral cortex. Preprint at eLife. https://doi.org/10.7554/eLife.92459.1.

14. Sergeant, J.A., Geurts, H., Huijbregts, S., Scheres, A., and Oosterlaan, J. (2003). The top and the bottom of ADHD: a neuropsychological perspective. Neurosci. Biobehav. Rev. *27*, 583–592. https://doi.org/10.1016/j.neubiorev.2003.08.004.

15. Maekawa, T., Tobimatsu, S., Inada, N., Oribe, N., Onitsuka, T., Kanba, S., and Kamio, Y. (2011). Top-down and bottom-up visual information processing of non-social stimuli in high-functioning autism spectrum disorder. Res. Autism Spectr. Disord. *5*, 201–209. https://doi.org/10.1016/j.rasd.2010.03.012.

16. Petrovic, P., and Castellanos, F.X. (2016). Top-down dysregulation—from ADHD to emotional instability. Front. Behav. Neurosci. *10*, 70. https://doi.org/10.3389/fnbeh.2016.00070.

17. Ursino, M., Serra, M., Tarasi, L., Ricci, G., Magosso, E., and Romei, V. (2022). Bottom-up vs. top-down connectivity imbalance in individuals with high-autistic traits: An electroencephalographic study. Front. Syst. Neurosci. *16*, 932128. https://doi.org/10.3389/fnsys.2022.932128.

18. Honey, C.J., Newman, E.L., and Schapiro, A.C. (2017). Switching between internal and external modes: A multiscale learning principle. Netw. Neurosci. *1*, 339–356. https://doi.org/10.1162/NETN_a_00024.

19. Christoff, K., Gordon, A.M., Smallwood, J., Smith, R., and Schooler, J.W. (2009). Experience sampling during fMRI reveals default network and executive system contributions to mind wandering. Proc. Natl. Acad. Sci. USA *106*, 8719–8724. https://doi.org/10.1073/pnas.0900234106.

20. Margulies, D.S., Ghosh, S.S., Goulas, A., Falkiewicz, M., Huntenburg, J.M., Langs, G., Bezgin, G., Eickhoff, S.B., Castellanos, F.X., Petrides, M., et al. (2016). Situating the default-mode network along a principal gradient of macroscale cortical organization. Proc. Natl. Acad. Sci. USA *113*, 12574–12579. https://doi.org/10.1073/pnas.1608282113.

21. Benedek, M., Jauk, E., Beaty, R.E., Fink, A., Koschutnig, K., and Neubauer, A.C. (2016). Brain mechanisms associated with internally directed attention and self-generated thought. Sci. Rep. *6*, 22959. https://doi.org/10.1038/srep22959.

22. Gu, Y., Sainburg, L.E., Kuang, S., Han, F., Williams, J.W., Liu, Y., Zhang, N., Zhang, X., Leopold, D.A., and Liu, X. (2021). Brain activity fluctuations propagate as waves traversing the cortical hierarchy. Cereb. Cortex *31*, 3986–4005. https://doi.org/10.1093/cercor/bhab064.

23. Raut, R.V., Snyder, A.Z., Mitra, A., Yellin, D., Fujii, N., Malach, R., and Raichle, M.E. (2021). Global waves synchronize the brain's functional systems with fluctuating arousal. Sci. Adv. *7*, eabf2709. https://doi.org/10.1126/sciadv.abf2709.

24. Bolt, T., Nomi, J.S., Bzdok, D., Salas, J.A., Chang, C., Thomas Yeo, B.T., Uddin, L.Q., and Keilholz, S.D. (2022). A parsimonious description of global functional brain organization in three spatiotemporal patterns. Nat. Neurosci. *25*, 1093–1103. https://doi.org/10.1038/s41593-022-01118-1.

25. Vinck, M., Oostenveld, R., Van Wingerden, M., Battaglia, F., and Pennartz, C.M. (2011). An improved index of phase-synchronization for electrophysiological data in the presence of volume-conduction, noise and sample-size bias. Neuroimage *55*, 1548–1565. https://doi.org/10.1016/j.neuroimage.2011.01.055.

26. Stam, C.J., and van Straaten, E.C. (2012). Go with the flow: use of a directed phase lag index (dPLI) to characterize patterns of phase relations in a large-scale model of brain dynamics. Neuroimage *62*, 1415–1428. https://doi.org/10.1016/j.neuroimage.2012.05.050.

27. VanRullen, R. (2016). Perceptual Cycles. Trends Cogn. Sci. *20*, 723–735. https://doi.org/10.1016/j.tics.2016.07.006.

28. Baker, A.P., Brookes, M.J., Rezek, I.A., Smith, S.M., Behrens, T., Probert Smith, P.J., and Woolrich, M. (2014). Fast transient networks in spontaneous human brain activity. eLife *3*, e01867. https://doi.org/10.7554/eLife.01867.

29. Lee, H., Golkowski, D., Jordan, D., Berger, S., Ilg, R., Lee, J., Mashour, G.A., Lee, U., Avidan, M.S., and Blain-Moraes, S. (2019). Relationship of critical dynamics, functional connectivity, and states of consciousness in large-scale human brain networks. Neuroimage *188*, 228–238. https://doi.org/10.1016/j.neuroimage.2018.12.011.

30. Telesford, Q.K., Gonzalez-Moreira, E., Xu, T., Tian, Y., Colcombe, S.J., Cloud, J., Russ, B.E., Falchier, A., Nentwich, M., Madsen, J., et al. (2023). An open-access dataset of naturalistic viewing using simultaneous EEG-fMRI. Sci. Data *10*, 554. https://doi.org/10.1038/s41597-023-02458-8.

31. Friedman-Hill, S.R., Wagman, M.R., Gex, S.E., Pine, D.S., Leibenluft, E., and Ungerleider, L.G. (2010). What does distractibility in ADHD reveal about mechanisms for top-down attentional control? Cognition *115*, 93–103. https://doi.org/10.1016/j.cognition.2009.11.013.

32. Kim, J., Moon, J.-Y., Lee, U., Kim, S., and Ko, T.-W. (2019). Various synchronous states due to coupling strength inhomogeneity and coupling functions in systems of coupled identical oscillators. Chaos *29*, 011106. https://doi.org/10.1063/1.5083621.

33. Woo, J.H., Lee, H.S., Moon, J.-Y., and Ko, T.-W. (2025). Hysteresis in a generalized Kuramoto model with a first-order approximate coupling function and inhomogeneous coupling strengths. Chaos Solitons Fractals *190*, 115770. https://doi.org/10.1016/j.chaos.2024.115770.

34. Davis, Z.W., Benigno, G.B., Fletterman, C., Desbordes, T., Steward, C., Sejnowski, T.J., H Reynolds, J., and Muller, L. (2021). Spontaneous traveling waves naturally emerge from horizontal fiber time delays and travel through locally asynchronous-irregular states. Nat. Commun. *12*, 6057. https://doi.org/10.1038/s41467-021-26175-1.

35. Koller, D.P., Schirner, M., and Ritter, P. (2024). Human connectome topology directs cortical traveling waves and shapes frequency gradients. Nat. Commun. *15*, 3570. https://doi.org/10.1038/s41467-024-47860-x.

36. Kim, M., Kim, H., Huang, Z., Mashour, G.A., Jordan, D., Ilg, R., and Lee, U. (2021). Criticality creates a functional platform for network transitions between internal and external processing modes in the human brain. Front. Syst. Neurosci. *15*, 657809. https://doi.org/10.3389/fnsys.2021.657809.

37. Daffertshofer, A., Ton, R., Kringelbach, M.L., Woolrich, M., and Deco, G. (2018). Distinct criticality of phase and amplitude dynamics in the resting brain. Neuroimage *180*, 442–447. https://doi.org/10.1016/j.neuroimage.2018.03.002.

38. Yeo, B.T., Krienen, F.M., Sepulcre, J., Sabuncu, M.R., Lashkari, D., Hollinshead, M., Roffman, J.L., Smoller, J.W., Zöllei, L., Polimeni, J.R., et al. (2011). The organization of the human cerebral cortex estimated by intrinsic functional connectivity. J. Neurophysiol. *106*, 1125–1165. https://doi.org/10.1152/jn.00338.2011.

39. Tripp, G., and Wickens, J.R. (2009). Neurobiology of ADHD. Neuropharmacology *57*, 579–589. https://doi.org/10.1016/j.neuropharm.2009.07.026.

40. Gallo, E.F., and Posner, J. (2016). Moving towards causality in attention-deficit hyperactivity disorder: overview of neural and genetic mechanisms. Lancet Psychiatry *3*, 555–567. https://doi.org/10.1016/S2215-0366(16)00096-1.

41. Faraone, S.V., Bellgrove, M.A., Brikell, I., Cortese, S., Hartman, C.A., Hollis, C., Newcorn, J.H., Philipsen, A., Polanczyk, G.V., Rubia, K., et al. (2024). Attention-deficit/hyperactivity disorder. Nat. Rev. Dis. Primers *10*, 11. https://doi.org/10.1038/s41572-024-00495-0.

42. Gonzalez-Gadea, M.L., Chennu, S., Bekinschtein, T.A., Rattazzi, A., Beraudi, A., Tripicchio, P., Moyano, B., Soffita, Y., Steinberg, L., Adolfi, F., et al. (2015). Predictive coding in autism spectrum disorder and attention deficit hyperactivity disorder. J. Neurophysiol. *114*, 2625–2636. https://doi.org/10.1152/jn.00543.2015.

43. Kwasa, J.A., Noyce, A.L., Torres, L.M., Richardson, B.N., and Shinn-Cunningham, B.G. (2023). Top-down auditory attention modulates neural responses more strongly in neurotypical than ADHD young adults. Brain Res. *1798*, 148144. https://doi.org/10.1016/j.brainres.2022.148144.

44. Alexander, L.M., Escalera, J., Ai, L., Andreotti, C., Febre, K., Mangone, A., Vega-Potler, N., Langer, N., Alexander, A., Kovacs, M., et al. (2017). An open resource for transdiagnostic research in pediatric mental health and learning disorders. Sci. Data *4*, 170181. https://doi.org/10.1038/sdata.2017.181.

45. Kaiser, A., Aggensteiner, P.-M., Baumeister, S., Holz, N.E., Banaschewski, T., and Brandeis, D. (2020). Earlier versus later cognitive event-related potentials (ERPs) in attention-deficit/hyperactivity disorder (ADHD): a meta-analysis. Neurosci. Biobehav. Rev. *112*, 117–134. https://doi.org/10.1016/j.neubiorev.2020.01.019.

46. Boxum, M., Voetterl, H., van Dijk, H., Gordon, E., DeBeus, R., Arnold, L.E., and Arns, M. (2025). Challenging the Diagnostic Value of Theta/Beta Ratio: Insights From an EEG Subtyping Meta-analytical Approach in ADHD. Appl. Psychophysiol. Biofeedback *50*, 655–666. https://doi.org/10.1007/s10484-024-09649-y.

47. Swanson, J., Deutsch, C., Cantwell, D., Posner, M., Kennedy, J.L., Barr, C.L., Moyzis, R., Schuck, S., Flodman, P., Spence, M.A., et al. (2001). Genes and attention-deficit hyperactivity disorder. Clin. Neurosci. Res. *1*, 207–216. https://doi.org/10.1016/S1566-2772(01)00007-X.

48. Shafiei, G., Markello, R.D., Makowski, C., Talpalaru, A., Kirschner, M., Devenyi, G.A., Guma, E., Hagmann, P., Cashman, N.R., Lepage, M., et al. (2020). Spatial patterning of tissue volume loss in schizophrenia reflects brain network architecture. Biol. Psychiatry *87*, 727–735. https://doi.org/10.1016/j.biopsych.2019.09.031.

49. Petras, K., Grabot, L., and Dugué, L. (2025). Locally Induced Traveling Waves Generate Globally Observable Traveling Waves. J. Neurosci. *45*, e0089252025. https://doi.org/10.1523/JNEUROSCI.0089-25.2025.

50. van Breugel, F., Kutz, J.N., and Brunton, B.W. (2020). Numerical Differentiation of Noisy Data: A Unifying Multi-Objective Optimization Framework. IEEE Access: Pract. Innov. Open Solut. *8*, 196865–196877. https://doi.org/10.1109/ACCESS.2020.3034077.

51. Chartrand, R. (2011). Numerical Differentiation of Noisy, Nonsmooth Data. Int. Sch. Res. Not. *2011*, 164564.

52. Palva, S., and Palva, J.M. (2011). Functional roles of alpha-band phase synchronization in local and large-scale cortical networks. Front. Psychol. *2*, 204. https://doi.org/10.3389/fpsyg.2011.00204.

53. Klimesch, W. (2012). Alpha-band oscillations, attention, and controlled access to stored information. Trends Cogn. Sci. *16*, 606–617. https://doi.org/10.1016/j.tics.2012.10.007.

54. Halgren, M., Ulbert, I., Bastuji, H., Fabó, D., Erőss, L., Rey, M., Devinsky, O., Doyle, W.K., Mak-McCully, R., Halgren, E., et al. (2019). The generation and propagation of the human alpha rhythm. Proc. Natl. Acad. Sci. USA *116*, 23772–23782. https://doi.org/10.1073/pnas.1913092116.

55. Musso, F., Brinkmeyer, J., Mobascher, A., Warbrick, T., and Winterer, G. (2010). Spontaneous brain activity and EEG microstates. A novel EEG/fMRI analysis approach to explore resting-state networks. NeuroImage *52*, 1149–1161. https://doi.org/10.1016/j.neuroimage.2010.01.093.

56. Britz, J., Van De Ville, D., and Michel, C.M. (2010). BOLD correlates of EEG topography reveal rapid resting-state network dynamics. NeuroImage *52*, 1162–1170. https://doi.org/10.1016/j.neuroimage.2010.02.052.

57. Yuan, H., Zotev, V., Phillips, R., Drevets, W.C., and Bodurka, J. (2012). Spatiotemporal dynamics of the brain at rest – exploring EEG microstates as electrophysiological signatures of BOLD resting state networks. NeuroImage *60*, 2062–2072. https://doi.org/10.1016/j.neuroimage.2012.02.031.

58. Britz, J., Van De Ville, D., and Michel, C.M. (2010). BOLD correlates of EEG topography reveal rapid resting-state network dynamics. NeuroImage *52*, 1162–1170. https://doi.org/10.1016/j.neuroimage.2010.02.052.

59. Yuan, H., Zotev, V., Phillips, R., Misaki, M., and Bodurka, J. (2018). fMRI resting-state networks link to EEG microstate dynamics in older adults. Front. Aging Neurosci. *10*, 366.

60. Xu, J., Pan, Y., Zhou, S., Zou, G., Liu, J., Su, Z., Zou, Q., and Gao, J.-H. (2020). EEG microstates are correlated with brain functional networks during slow-wave sleep. NeuroImage *215*, 116786. https://doi.org/10.1016/j.neuroimage.2020.116786.

61. Rajkumar, R., Farrher, E., Mauler, J., Sripad, P., Régio Brambilla, C.R., Rota Kops, E., Scheins, J., Dammers, J., Lerche, C., Langen, K.-J., et al. (2021). Comparison of EEG microstates with resting state fMRI and FDG-PET measures in the default mode network via simultaneously recorded trimodal (PET/MR/EEG) data. Hum. Brain Mapp. *42*, 4122–4133. https://doi.org/10.1002/hbm.24429.

62. Sergeant, J.A. (2005). Modeling attention-deficit/hyperactivity disorder: a critical appraisal of the cognitive-energetic model. Biol. Psychiatry *57*, 1248–1255. https://doi.org/10.1016/j.biopsych.2004.09.010.

63. Nigg, J.T., and Casey, B.J. (2005). An integrative theory of attention-deficit/ hyperactivity disorder based on the cognitive and affective neurosciences. Dev. Psychopathol. *17*, 785–806. https://doi.org/10.1017/S0954579405050376.

64. Hinshaw, S.P. (2018). Attention deficit hyperactivity disorder (ADHD): controversy, developmental mechanisms, and multiple levels of analysis. Annu. Rev. Clin. Psychol. *14*, 291–316. https://doi.org/10.1146/annurev-clinpsy-050817-084917.

65. van den Heuvel, M.P., and Sporns, O. (2011). Rich-club organization of the human connectome. J. Neurosci. *31*, 15775–15786. https://doi.org/10.1523/JNEUROSCI.3539-11.2011.

66. Honey, C.J., Sporns, O., Cammoun, L., Gigandet, X., Thiran, J.P., Meuli, R., and Hagmann, P. (2009). Predicting human resting-state functional connectivity from structural connectivity. Proc. Natl. Acad. Sci. USA *106*, 2035–2040. https://doi.org/10.1073/pnas.0811168106.

67. Zou, W., Senthilkumar, D.V., Nagao, R., Kiss, I.Z., Tang, Y., Koseska, A., Duan, J., and Kurths, J. (2015). Restoration of rhythmicity in diffusively coupled dynamical networks. Nat. Commun. *6*, 7709. https://doi.org/10.1038/ncomms8709.

68. Woo, J.H., Honey, C.J., and Moon, J.-Y. (2020). Phase and amplitude dynamics of coupled oscillator systems on complex networks. Chaos *30*, 121102. https://doi.org/10.1063/5.0031031.

69. Kopell, N., and Ermentrout, B. (2004). Chemical and electrical synapses perform complementary roles in the synchronization of interneuronal networks. Proc. Natl. Acad. Sci. USA *101*, 15482–15487. https://doi.org/10.1073/pnas.0406343101.

70. Pereda, A.E. (2014). Electrical synapses and their functional interactions with chemical synapses. Nat. Rev. Neurosci. *15*, 250–263. https://doi.org/10.1038/nrn3708.

71. Megam Ngouonkadi, E.B., Fotsin, H.B., and Louodop Fotso, P.H. (2014). The combined effect of dynamic chemical and electrical synapses in time-delay-induced phase-transition to synchrony in coupled bursting neurons. Int. J. Bifürcation Chaos *24*, 1450069. https://doi.org/10.1142/S0218127414500692.

72. Wang, J., Guo, X., Yu, H., Liu, C., Deng, B., Wei, X., and Chen, Y. (2014). Stochastic resonance in small-world neuronal networks with hybrid electrical–chemical synapses. Chaos Solitons Fractals *60*, 40–48. https://doi.org/10.1016/j.chaos.2014.01.005.

73. Pang, J.C., Aquino, K.M., Oldehinkel, M., Robinson, P.A., Fulcher, B.D., Breakspear, M., and Fornito, A. (2023). Geometric Constraints on Human Brain Function. Nature *618*, 566–574. https://doi.org/10.1038/s41586-023-06098-1.

74. Cruddas, J., Pang, J.C., and Fornito, A. (2026). Cortical Traveling Waves in Time and Space: Physics, Physiology, and Psychology. Neuron *114*, 985–1005. https://doi.org/10.1016/j.neuron.2025.12.019.

75. Huang, X., Troy, W.C., Yang, Q., Ma, H., Laing, C.R., Schiff, S.J., and Wu, J.-Y. (2004). Spiral Waves in Disinhibited Mammalian Neocortex. J. Neurosci. *24*, 9897–9902. https://doi.org/10.1523/JNEUROSCI.2705-04.2004.

76. Huang, X., Xu, W., Liang, J., Takagaki, K., Gao, X., and Wu, J.-Y. (2010). Spiral Wave Dynamics in Neocortex. Neuron *68*, 978–990. https://doi.org/10.1016/j.neuron.2010.11.007.

77. Bonnefond, M., and Jensen, O. (2012). Alpha oscillations serve to protect working memory maintenance against anticipated distracters. Curr. Biol. *22*, 1969–1974. https://doi.org/10.1016/j.cub.2012.08.029.

78. Bekinschtein, T.A., Dehaene, S., Rohaut, B., Tadel, F., Cohen, L., and Naccache, L. (2009). Neural signature of the conscious processing of auditory regularities. Proc. Natl. Acad. Sci. USA *106*, 1672–1677. https://doi.org/10.1073/pnas.0809667106.

79. Wacongne, C., Labyt, E., Van Wassenhove, V., Bekinschtein, T., Naccache, L., and Dehaene, S. (2011). Evidence for a hierarchy of predictions and prediction errors in human cortex. Proc. Natl. Acad. Sci. USA *108*, 20754–20759. https://doi.org/10.1073/pnas.1117807108.

80. Chao, Z.C., Takaura, K., Wang, L., Fujii, N., and Dehaene, S. (2018). Large-scale cortical networks for hierarchical prediction and prediction error in the primate brain. Neuron *100*, 1252–1266.e3. https://doi.org/10.1016/j.neuron.2018.10.004.

81. Marr, D. (1982). Vision: A Computational Investigation into the Human Representation and Processing of Visual Information. https://people.ciirc.cvut.cz/~hlavac/pub/MiscTextForStudents/1982MarrDavidVisionBook.pdf.

82. Love, B.C. (2015). The algorithmic level is the bridge between computation and brain. Top. Cogn. Sci. *7*, 230–242. https://doi.org/10.1111/tops.12131.

83. Park, Y. youngjai/RelativePhaseAnalysis. (2025). Github. https://github.com/youngjai/RelativePhaseAnalysis.

84. Moon, J.-Y. RelativePhaseAnalysis. (2026). Github. https://github.com/onemoon4u/RelativePhaseAnalysis.

85. Delorme, A., and Makeig, S. (2004). EEGLAB: an open source toolbox for analysis of single-trial EEG dynamics including independent component analysis. J. Neurosci. Methods *134*, 9–21. https://doi.org/10.1016/j.jneumeth.2003.10.009.

86. Cragg, L., Kovacevic, N., McIntosh, A.R., Poulsen, C., Martinu, K., Leonard, G., and Paus, T. (2011). Maturation of EEG power spectra in early adolescence: a longitudinal study. Dev. Sci. *14*, 935–943. https://doi.org/10.1111/j.1467-7687.2010.01031.x.

87. Telesford, Q., Franco, A.R., Milham, M., Schroeder, C., Telesford, Q.K., Gonzalez-Moreira, E., Xu, T., Tian, Y., Colcombe, S., Cloud, J., et al. (2024). EEG/FMRI Naturalistic Viewing Dataset. https://fcon_1000.projects.nitrc.org/indi/retro/nat_view.html.

88. Xu, T., Yang, Z., Jiang, L., Xing, X.-X., and Zuo, X.-N. (2015). A connectome computation system for discovery science of brain. Sci. Bull. *60*, 86–95. https://doi.org/10.1007/s11434-014-0698-3.

89. Schaefer, A., Kong, R., Gordon, E.M., Laumann, T.O., Zuo, X.-N., Holmes, A.J., Eickhoff, S.B., and Yeo, B.T. (2018). Local-global parcellation of the human cerebral cortex from intrinsic functional connectivity MRI. Cereb. Cortex *28*, 3095–3114. https://doi.org/10.1093/cercor/bhx179.

90. Freeman, W.J. (2007). Hilbert transform for brain waves. Scholarpedia *2*, 1338. https://doi.org/10.4249/scholarpedia.1338.

91. Forgy, E.W. (1965). Cluster analysis of multivariate data: efficiency versus interpretability of classifications. Biometrics *21*, 768–769.

92. Pelleg, D., and Moore, A. (1999). Accelerating exact k-means algorithms with geometric reasoning. In Proceedings of the fifth ACM SIGKDD international conference on Knowledge discovery and data mining, pp. 277–281.

93. Davies, D.L., and Bouldin, D.W. (1979). A cluster separation measure. IEEE Trans. Pattern Anal. Mach. Intell. *1*, 224–227. https://doi.org/10.1109/TPAMI.1979.4766909.

94. Freedman, D.A. (2009). A simple regression equation has on the right-hand side an intercept and an explanatory variable with a slope coefficient. A multiple regression e right hand side, each with its own slope coefficient. Statistical Models. Theory Pract. 26.

95. Stewart, G.W. (1993). On the early history of the singular value decomposition. SIAM Rev. *35*, 551–566. https://doi.org/10.1137/1035134.

96. Jolliffe, I.T., and Cadima, J. (2016). Principal component analysis: a review and recent developments. Philos. Trans. A Math. Phys. Eng. Sci. *374*, 20150202. https://doi.org/10.1098/rsta.2015.0202.

97. Eriksen, K.A., Simonsen, I., Maslov, S., and Sneppen, K. (2003). Modularity and extreme edges of the Internet. Phys. Rev. Lett. *90*, 148701. https://doi.org/10.1103/PhysRevLett.90.148701.

98. Beugeling, W., Andreanov, A., and Haque, M. (2015). Global characteristics of all eigenstates of local many-body Hamiltonians: participation ratio and entanglement entropy. J. Stat. Mech.: Theory Exp. *2015*, P02002. https://doi.org/10.1088/1742-5468/2015/02/P02002.

99. Ding, C., and He, X. (2004). K-means clustering via principal component analysis. In Proceedings of the twenty-first international conference on Machine learning (ACM Press), pp. 29. https://doi.org/10.1145/1015330.1015408.

100. Dunn, J.C. (1973). A fuzzy relative of the ISODATA process and its use in detecting compact well-separated clusters. J. Cybern. *3*, 32–57. https://doi.org/10.1080/01969727308546046.

101. Honey, C.J., and Sporns, O. (2008). Dynamical consequences of lesions in cortical networks. Hum. Brain Mapp. *29*, 802–809. https://doi.org/10.1002/hbm.20579.

102. Deco, G., Jirsa, V., McIntosh, A.R., Sporns, O., and Kötter, R. (2009). Key role of coupling, delay, and noise in resting brain fluctuations. Proc. Natl. Acad. Sci. USA *106*, 10302–10307. https://doi.org/10.1073/pnas.0901831106.

103. Breakspear, M., Heitmann, S., and Daffertshofer, A. (2010). Generative models of cortical oscillations: neurobiological implications of the Kuramoto model. Front. Hum. Neurosci. *4*, 190. https://doi.org/10.3389/fnhum.2010.00190.

104. Schmidt, R., LaFleur, K.J., de Reus, M.A., van den Berg, L.H., and van den Heuvel, M.P. (2015). Kuramoto model simulation of neural hubs and dynamic synchrony in the human cerebral connectome. BMC Neurosci. *16*, 54. https://doi.org/10.1186/s12868-015-0193-z.

105. Finger, H., Bönstrup, M., Cheng, B., Messé, A., Hilgetag, C., Thomalla, G., Gerloff, C., and König, P. (2016). Modeling of large-scale functional brain networks based on structural connectivity from DTI: comparison with EEG derived phase coupling networks and evaluation of alternative methods along the modeling path. PLoS Comput. Biol. *12*, e1005025. https://doi.org/10.1371/journal.pcbi.1005025.

106. Kim, M., Kim, S., Mashour, G.A., and Lee, U. (2017). Relationship of topology, multiscale phase synchronization, and state transitions in human

brain networks. Front. Comput. Neurosci. *11*, 55. https://doi.org/10.3389/fncom.2017.00055.

107. Fukushima, M., and Sporns, O. (2018). Comparison of fluctuations in global network topology of modeled and empirical brain functional connectivity. PLoS Comput. Biol. *14*, e1006497. https://doi.org/10.1371/journal.pcbi.1006497.
108. Petkoski, S., Palva, J.M., and Jirsa, V.K. (2018). Phase-lags in large scale brain synchronization: Methodological considerations and in-silico analysis. PLoS Comput. Biol. *14*, e1006160. https://doi.org/10.1371/journal.pcbi.1006160.
109. Kashyap, A., and Keilholz, S. (2019). Dynamic properties of simulated brain network models and empirical resting-state data. Netw. Neurosci. *3*, 405–426. https://doi.org/10.1162/netn_a_00070.
110. Ódor, G., and Kelling, J. (2019). Critical synchronization dynamics of the Kuramoto model on connectome and small world graphs. Sci. Rep. *9*, 19621. https://doi.org/10.1038/s41598-019-54769-9.
111. Ódor, G., Gastner, M.T., Kelling, J., and Deco, G. (2021). Modelling on the very large-scale connectome. J. Phys. Complex. *2*, 045002. https://doi.org/10.1088/2632-072X/ac266c.
112. Pope, M., Fukushima, M., Betzel, R.F., and Sporns, O. (2021). Modular origins of high-amplitude cofluctuations in fine-scale functional connectivity dynamics. Proc. Natl. Acad. Sci. UA *118*, e2109380118. https://doi.org/10.1073/pnas.2109380118.
113. Deco, G., Liebana Garcia, S., Sanz Perl, Y., Sporns, O., and Kringelbach, M.L. (2023). The effect of turbulence in brain dynamics information transfer measured with magnetoencephalography. Commun. Phys. *6*, 74. https://doi.org/10.1038/s42005-023-01192-2.
114. Pope, M., Seguin, C., Varley, T.F., Faskowitz, J., and Sporns, O. (2023). Co-evolving dynamics and topology in a coupled oscillator model of resting brain function. NeuroImage *277*, 120266. https://doi.org/10.1016/j.neuroimage.2023.120266.
115. Griffa, A., Alemán-Gómez, Y., and Hagmann, P. (2019). Structural and functional connectome from 70 young healthy adults. Zenodo. https://zenodo.org/records/2872624.
116. Shafiei, G., Markello, R., Talpalaru, T., Makowski, C., Kirschner, M., Devenyi, G.A., Hagmann, P., Cashman, N.R., Lepage, M., Chakravarty, M.M., et al. (2019). Consensus Structural and functional connectome from 70 young healthy adults. Zenodo. https://zenodo.org/records/3067849.
117. Mišić, B., Betzel, R.F., Nematzadeh, A., Goñi, J., Griffa, A., Hagmann, P., Flammini, A., Ahn, Y.-Y., and Sporns, O. (2015). Cooperative and competitive spreading dynamics on the human connectome. Neuron *86*, 1518–1529. https://doi.org/10.1016/j.neuron.2015.05.035.
118. Betzel, R.F., Griffa, A., Hagmann, P., and Mišić, B. (2019). Distance-dependent consensus thresholds for generating group-representative structural brain networks. Netw. Neurosci. *3*, 475–496. https://doi.org/10.1162/netn_a_00075.
119. Ko, T.-W., and Ermentrout, G.B. (2008). Bistability between synchrony and incoherence in limit-cycle oscillators with coupling strength inhomogeneity. Phys. Rev. E Stat. Nonlin. Soft Matter Phys. *78*, 026210. https://doi.org/10.1103/PhysRevE.78.026210.
120. Uhlenbeck, G.E., and Ornstein, L.S. (1930). On the theory of the Brownian motion. Phys. Rev. *36*, 823–841. https://doi.org/10.1103/PhysRev.36.823.
121. Moreno-Bote, R., and Parga, N. (2006). Auto- and Crosscorrelograms for the Spike Response of Leaky Integrate-and-Fire Neurons with Slow Synapses. Phys. Rev. Lett. *96*, 028101. https://doi.org/10.1103/PhysRevLett.96.028101.
122. Wong, K.-F., and Wang, X.-J. (2006). A recurrent network mechanism of time integration in perceptual decisions. J. Neurosci. *26*, 1314–1328. https://doi.org/10.1523/JNEUROSCI.3733-05.2006.
123. Touboul, J., and Destexhe, A. (2017). Power-law statistics and universal scaling in the absence of criticality. Phys. Rev. E *95*, 012413. https://doi.org/10.1103/PhysRevE.95.012413.
124. Gilson, M., Zamora-López, G., Pallarés, V., Adhikari, M.H., Senden, M., Campo, A.T., Mantini, D., Corbetta, M., Deco, G., and Insabato, A. (2020). Model-based whole-brain effective connectivity to study distributed cognition in health and disease. Netw. Neurosci. *4*, 338–373. https://doi.org/10.1162/netn_a_00117.
125. Gilson, M., Tagliazucchi, E., and Cofré, R. (2023). Entropy production of multivariate Ornstein-Uhlenbeck processes correlates with consciousness levels in the human brain. Phys. Rev. E *107*, 024121. https://doi.org/10.1103/PhysRevE.107.024121.
126. Strogatz, S.H. (2018). Nonlinear dynamics and chaos: with applications to physics, biology, chemistry, and engineering (CRC Press).

STAR★METHODS

KEY RESOURCES TABLE

REAGENT or RESOURCE	SOURCE	IDENTIFIER
Software and algorithms		
MATLAB R2024b	MathWorks	https://kr.mathworks.com/products/matlab.html
EEGLAB v24.2.1.	Delorme and Makeig[85]	https://doi.org/10.1016/j.jneumeth.2003.10.009
Deposited data		
Healthy Brain Network data set	Alexander et al.[44]	https://fcon_1000.projects.nitrc.org/indi/cmi_healthy_brain_network/
Nathan Kline Institute data set	Telesford et al.[30]	https://fcon_1000.projects.nitrc.org/indi/retro/nat_view.html
Other		
UofM and Healthy Brain Network EEG	128-channel HydroCel Geodesic Sensor Net with Net Amps 400 amplifier from Electrical Geodesic, Inc. (EGI)	N/A
Nathan Kline Institute fMRI	3T Siemens TrioTim	N/A
Nathan Kline Institute EEG	Brain Products BrainCapMR[64] channels	N/A

EXPERIMENTAL MODEL AND STUDY PARTICIPANT DETAILS

In this section, we describe the details of the datasets used in our analyses and the preprocessing pipelines. We used three datasets.

General anesthesia EEG data (UofM: University of Michigan)

EEG recordings from eighteen healthy volunteers (20-40 years old) were collected at the University of Michigan.[29,36] The study was reviewed in accordance with the recommendations of the Institutional Review Boards specializing in human subject research at the University of Michigan, Ann Arbor (Protocol #HUM0071578). Written informed consent was obtained from all participants in accordance with the Declaration of Helsinki. Nine participants underwent general anesthesia, the others were recorded without anesthesia. EEG data were recorded with 128-channel HydroCel nets, Net Amps 400 amplifiers (Electrical Geodesic, Inc., USA) at a sampling rate of 500 Hz. The location of the reference channel was at Cz.

The experimental paradigm was designed to simulate the conditions of general anesthesia typically used in a surgical setting. Participants in the anesthesia group initially received propofol through increasing infusion rates over three consecutive 5-minute blocks: Block 1 (100 μg/kg/min), Block 2 (200 μg/kg/min), and Block 3 (300 μg/kg/min). Responsiveness was assessed every 30 seconds using the verbal command, "Squeeze your left/right hand twice," with left/right assignment randomized. Following this, isoflurane was administered with air and 40% oxygen at 1.3 age-adjusted minimum alveolar concentration (MAC). Isoflurane was maintained for 3 hours before being discontinued.

Resting vs. checkerboard task from simultaneous EEG-fMRI data (NKI: Nathan Kline Institute)

We used simultaneous EEG-fMRI recordings from the NKI dataset to compare EEG relative phase dynamics with task-evoked BOLD responses during resting-state and flashing-checkerboard stimulation periods.

The dataset is collected at the NKI (Nathan Kline Institute).[30] The recordings were obtained from 22 individuals between the ages of 23 and 51 years old. EEG data contains 64-channels using a customized Brain Products (BrainCapMR consisting of 61 cortical channels, two EOG channels placed below (channel 63) and above (channel 64) the left eye, and one ECG channel (channel 32)). The location of the reference channel was at FCz. All individuals were consented in accordance and compliance with the Institutional Review Board (IRB) at NKI. fMRI data was acquired using a 12-channel head coil on 3T Siemens TIM Trio. All BOLD fMRI sequences were acquired with these following parameters: TR=2100ms; TE=24.6ms; slices=38; matrix size=64 × 64; voxel size=3.469 × 3.469 × 3.330mm^3.

ADHD/Control EEG data (HBN: Healthy Brain Network)

To analyze the differences in the directionality of phase relationship between the ADHD group and the control group, we used eyes closed and eyes open resting state data from the Healthy Brain Network (HBN) dataset released by the Child Mind Institute.[44] The HBN dataset is a large-scale data collection targeting adolescents (aged 5-21) living in the New York City area. It consists of extensive

multimodal datasets covering a wide spectrum of commonly encountered clinical psychopathologies including attention deficit hyperactivity disorder (ADHD). To examine the real-time directionality of phase relationship across whole brain regions, we used high-density electroencephalography (EEG) data recorded at a sampling rate of 500 Hz using a 128-channel geodesic hydrocel system by Electrical Geodesics Inc. The location of the reference channel was at Cz.

To establish a more robust sample with ADHD-Inattentive type, we selected individuals who had been diagnosed with ADHD inattentive type without comorbidity. The control group consists of individuals who had not received any diagnosis. The EEG signal in the alpha spectrum peak shows a qualitative difference between age under and above 10.[86] Therefore, we chose individuals aged 11 and older. In conclusion, resting state data from a total of 53 ADHD participants (41 male, mean age 14.11, standard error (s.e.) 0.27) and 88 control individuals (44 male, mean age 14.07, s.e. 0.28) were used for the analysis. Participants are encouraged to discontinue stimulant medication due to its potential effects on cognitive and behavioral testing and brain function mapping.[44] However, those who choose not to or are required by their physicians to continue medication can still participate, with their medication intake recorded on the day of the study. Three participants in the selected ADHD-inattentive group were on medication during data collection, and they were not excluded from the analysis; given this small subsample, we did not perform statistical comparisons by medication status.

METHOD DETAILS

This section first describes dataset-specific preprocessing and state extraction procedures, followed by the Relative Phase Analysis (RPA) framework and the additional measures used for comparison with RPA.

As outlined in the Figure 6, RPA pipeline consists of the following steps: (i) apply the Hilbert transform to the EEG time series to extract the instantaneous phase; (ii) compute the relative phase, yielding the relative phase map for each time point, across time; (iii) apply either *K*-means clustering or principal component analysis (PCA) to identify dominant spatial patterns (centroids or PCs, which are approximately equivalent); (iv) perform linear regression using these centroids or PCs as regressors to compute dynamic regression coefficients; (v) the resulting coefficient time series were analyzed to characterize the temporal expression of dominant relative phase modes and their associated statistics.

Each step is described in more detail in the following subsections.

EEG state extraction for the UofM general anesthesia dataset

In the EEG data, we extracted 5-minute eyes-open and 5-minute *eyes-closed* resting states from the no anesthesia group (nine subjects). In the general anesthesia group (nine subjects), we extracted five types of brain states over time to study differences among the different brain states; 1) 5-minute *eyes-closed* resting state before general anesthesia, 2) 3-minute *LOC* (loss of consciousness) state after LOC marker, 3) *burst* state pieces with a total of 5-minute, 4) *suppression* state pieces with a total of 5-minute, and 5) 5-minute *ROC* (recovery of consciousness) state after ROC marker. LOC and ROC markers in the EEG data were measured by responding to the verbal command (“Squeeze your left/right hand twice” with left/right randomized) every 30 seconds[29]. In the data, six subjects of the anesthesia group showed burst and suppression states under anesthesia. The burst state is a period when the power in the spectrogram suddenly increases across all frequency bands even though the subjects are under anesthesia. On the contrary, in the suppression state, the power remains extremely low. In particular, we manually extracted the burst and suppression states because it is unclear to quantitatively define the states. To increase sample size for state comparisons, we divided the data into 1-minute segments and analyzed them.

Preprocessing of the NKI fMRI dataset

In fMRI BOLD signals, we use the preprocessed data served by the reference site[30,87,88] (func_pp_filter_gsr_sm0.mni152.3mm.nii.gz). Briefly, the structural preprocessing included skull-stripping, tissue segmentation (gray matter, white matter, cerebrospinal fluid), and registration to the MNI152 template. The functional preprocessing included slice timing, motion correction, boundary-based co-registration, nuisance regression (Friston’s 24 head motion parameters, white matter, cerebrospinal fluid, and global signal), band-pass filter (0.01-0.1 Hz) and linear and quadratic detrending . For spatial averaging under the 1,000-parcel Schaefer parcellation scheme,[89] fMRI volumes were resampled to 2 mm isotropic resolution to align with the parcellation template. Voxel-level time series were then averaged within each parcel, and the resulting parcel-wise time series were Z-scored across time to normalize voxel-specific signal variability. The Z-scored time series were then averaged across trials and participants to derive group-level time series. Finally, the difference between group-averaged signals during rest and the flashing checkerboard stimulation periods was computed in our analysis.

We note that to account for delayed hemodynamic and electrophysiological responses, event onsets of the flashing checkerboard stimuli were shifted by 6 seconds–effectively aligning event boundaries 6 seconds later relative to the recorded BOLD and EEG signals. Cross-correlation between BOLD response and EEG relative phase dynamics (represented by β_1) peaked at zero lag, indicating a strong temporal correspondence between the two signals. This suggests that the group-averaged EEG relative phase dynamics is not only correlated with BOLD signals but may also exhibit similar delays relative to event onsets, reflecting shared latency in their response to external stimuli.

Preprocessing of HBN EEG dataset

For the preprocessing procedure, we used the EEGLAB package in MATLAB.[85] The EEG signal was processed as follows: 1) notch filtered at 60 Hz to remove power line noise, 2) bad channels were detected and removed using the trimOutlier.m function, and 3) band-pass filtered across six frequency bands (delta: 1-4 Hz, theta: 4-8 Hz, alpha: 8-12 Hz, low beta: 12-20 Hz, high beta: 20-30 Hz, gamma: 30-50 Hz). We analyzed EEG signals in the original recording reference provided with each dataset and did not apply additional re-referencing. To remove excessively noisy channels, we used the EEGLAB trimOutlier. This procedure computes a channel-wise variability metric by dividing the continuous data into 100 equal-length bins, computing the standard deviation within each bin for each channel, and averaging these values across bins to obtain a mean SD per channel. Channels whose mean SD fell outside the specified bounds ($< 10^{-4}$ or > 100) were removed.

Relative Phase Analysis of EEG signals

EEG signals can be decomposed into amplitude and phase components over time using the Hilbert transform.[90] The phase of each electrode reflects the specific timing of its signal within a periodic waveform. To determine the directionality of information flow, we use the relative phase, which is derived by subtracting the global mean phase from the phase of each electrode.[5,7] In the following equations, θ_j represents the signal phase of j^{th} electrode, and Θ denotes the system's mean phase:

$$Re^{i\Theta} = \frac{1}{N}\sum_{j=1}^{N} e^{i\theta_j}, \quad \text{(Equation 1)}$$

$$\sin\phi_j = \sin\left(\theta_j - \Theta\right). \quad \text{(Equation 2)}$$

Here, Equation 1 represents the global mean phase and Equation 2 represents the relative phase. Equation 1 defines the system's phase denoted as Θ, which represents the global mean phase of the system at each time point, capturing the brain's overall phase state. In Equation 2, we subtract the system's phase from each signal's phase. When ϕ_j is a positive value, the signal from an electrode leads the global mean phase, whereas a negative value indicates that it lags the global mean phase. Finally, we weighted the resulting phase difference by applying the sine function, mapping the values continuously from -1 to $+1$. This is our definition of relative phase for channel j. In this framework, -1 corresponds to a 90° phase lag, $+1$ to a 90° phase lead, and 0 is obtained for phase differences of 0° or 180°. This weighting strategy is inspired by phase-based measures that mitigate the heightened sensitivity to noise—arising from factors such as volume conduction—near 0° and 180° differences in phase-lead/lag calculations.[25] Using our approach, we can reliably estimate whether j is relatively phase-leading or lagging compared to the system's average phase at each time point.

Choosing the optimal temporal scale of RPA

In performing Relative Phase Analysis (RPA), we determined the optimal time scale for capturing dynamics by calculating Shannon entropy of the relative phase time series (Figure S2A). We observed that the Shannon entropy of relative phase—computed over time windows of varying sizes—decreases as the window size increases across all frequency bands, indicating that the diversity of relative phase patterns diminishes with broader time averaging (We note that the Shannon entropy of relative phase was computed for each channel first then averaged over all channels). Notably, the alpha band (8–12 Hz) retains its Shannon entropy over longer time scales compared to other bands, up to approximately 100 ms (equivalent to a 10 Hz sampling rate), suggesting that 100 ms is a characteristic time scale for its relative phase patterns. Consequently, in our main analysis, we focus on the alpha wave's relative phase time series downsampled to 10 Hz (equivalent to time resolution of 100ms) to examine brain-state-dependent characteristics. We further note that increasing the downsampling rate to 50 Hz (yielding a time resolution of 20 ms) produces transition dynamics results that are highly consistent (Figures S4 and S5).

K-means clustering of the relative phase patterns

The relative phase in the brain shows distinct patterns over time, reflecting different brain states. We found that the dynamics of the relative phase patterns show different aspects depending on the brain states. Interestingly, these patterns are not random in conscious states but follow specific dynamics. The *K*-means clustering algorithm finds dominant patterns as centroids by iteration in a given dataset.[91,92] We performed *K*-means clustering to find dominant relative phase topographic patterns in the dynamics.

K-means clustering divides the given data into *K* clusters, a parameter that must be predetermined. To determine the optimal *K* for resting state brain patterns, we evaluate the clustering performance using the Davies-Bouldin Index (DBI).[93] The DBI reflects clustering quality, with higher values when the average distance between the same cluster is greater than the average distance between different clusters, otherwise lower values. After examining the DBI values across varying *K* values, we found that the optimal number of clusters for the brain's resting state is $K = 4$ (Figure S3A).

In the main text, we applied RPA across different groups or brain states. In the investigation, we identified universal relative phase patterns based on resting state data. We derived four centroids using *K*-means clustering from two datasets: the concatenated resting state recordings of 18 subjects from the University of Michigan (UofM), and the concatenated resting state recordings of the Healthy Brain Network (HBN) control group (66 subjects), respectively. We excluded the NKI dataset due to noise introduced by simultaneous fMRI-EEG recordings. Despite analyzing different datasets, we found that the same four centroids emerged

consistently: i) front-leading/back-lagging pattern (mode 1), ii) left-leading/right-lagging pattern (mode 2), iii) right-leading/left-lagging pattern (mode 3), iv) back-leading/front-lagging pattern (mode 4) (Figure 1B). Therefore, we analyzed relative phase dynamics using these four centroids as the standard. We note that mode 1 and mode 4 are almost anti-symmetric to each other, as with mode 2 and mode 3.

Linear regression using the centroids as regressors

The *K*-means clustering algorithm assigns every time frame to one of the four modes, even if some ambiguous frames do not closely resemble any mode. This limitation introduces ambiguity, as frames that fall between distinct patterns are still forced into one cluster. To address this issue, we performed multiple linear regression with the universal centroids identified with the K-means clustering[94] as regressors. Unlike *K*-means clustering, which provides binary assignments, multiple linear regression assigns continuous weights to each mode for every time frame, representing the contribution of each pattern more accurately.

For every time series of relative phase topographic maps, such linear regression (taking the centroids of the *K*-means clustering as the vector of regressors) can be performed. The relative phase topographic map of each time point becomes the dependent variable $\widehat{y}(t)$ (Figure 1C):

$$\widehat{\boldsymbol{y}}(t) = \beta_1(t)\cdot X_1 + \beta_2(t)\cdot X_2 + \varepsilon(t), \quad \text{(Equation 3)}$$

where $\widehat{\boldsymbol{y}}$ is the relative phase pattern at a given time t, X_1 and X_2 are regressors based on the previously identified centroids. The first regressor is the centroid representing front-to-back pattern (negative of which represent back-to-front pattern), and the second vector is a centroid representing left-to-right (negative of which represent right-to-left pattern) (Figures 1C, S1B, and S1C). By observing how the coefficients for the first and second vector ($\beta_1(t)$ and $\beta_2(t)$ respectively) change over time, we can quantify the dominance of each mode. ε represents residuals that cannot be explained by the superposition of X_1 and X_2.

We note that such linear regression approach is approximately equivalent to principal component analysis (PCA), and the resulting clustering closely aligns with the *K*-means clustering results (Figure 1B). This equivalence arises from the inherent relationship between *K*-means clustering and PCA, where each principal component closely corresponds to two paired modes identified by *K*-means clustering.

Quantifying brain states is challenging because both the relative phase time series and traditional measurements are calculated for each channel. Conventional approaches often reduce the dimension of the time series by averaging the measurements across channels, even though this approach may overlook spatially specific brain activity. In contrast, our approach preserves spatial information by focusing on temporal patterns without averaging over channels. In summary, we can obtain three distinct coefficient time series (i.e. β_1, β_2, and $|\varepsilon|$) using multiple linear regression with the universal centroids.

Principal Component Analysis (PCA) of relative phase dynamics

Principal component analysis (PCA) is a linear dimensionality reduction technique that finds the dominant axes of variation from a given dataset.[95,96] By applying PCA, we can obtain the principal components, with each component explaining a proportion of the total variance along its corresponding axis. The inverse Participation Ratio (iPR) is defined as the following:

For a eigenvector $\boldsymbol{v} = (v_1, v_2, \ldots, v_N)$:

$$IPR\,(v) = \frac{\sum_{i=1}^{N} |v_i|^4}{\left(\sum_{i=1}^{N} |v_i|^2\right)^2} \quad \text{(Equation 4)}$$

The inverse participation ratio (iPR) provides a measure of how unevenly variance is distributed across components: a high iPR indicates localization onto a few dominant components, while a low iPR indicates broader participation.[97,98] By inverting the iPR, the participation ratio (PR) estimates the effective number of principal axes that significantly contribute to variance. This measure enables direct comparison of the dimensionality of brain dynamics across states.

As described in the previous section, our linear regression approach is mathematically equivalent to principal component analysis (PCA). When the regressors in the linear regression are chosen as the principal components of the relative phase topographic maps, the resulting coefficients ($\beta_1(t)$ and $\beta_2(t)$ in our case) correspond to the coordinates of the relative phase topographic maps in the principal component space. The relationship between linear regression, K-means clustering, and PCA has been previously studied and established[99]: it was shown that the centroids produced by *K*-means clustering approximately span the first $K = 1$ principal components. The principal components closely resemble the centroids from the K-means clustering. To validate the robustness of our findings, we applied all three methods (linear regression, *K*-means clustering, and PCA) and cross-checked the consistency of the results across techniques.

Statistics over brain states

By applying multiple linear regression and comparing whether $|\beta_1|$ is larger than $|\beta_2|$, we can obtain an index for each time frame. This index indicates the similarity to specific modes; i) mode 1 (front-leading/back-lagging, i.e. positive sign of β_1), ii) mode 2 (left-leading/right-lagging, i.e. positive sign of β_2), iii) mode 3 (right-leading/left-lagging, i.e. negative sign of β_2), iv) mode 4 (back-leading/front-lagging, i.e. negative sign of β_1). Using these indices, we can construct a probability density function to calculate the mode

distribution over different brain states. In addition, by weighting each time frame with its corresponding regression coefficient, we can better distinguish the brain states (Figures S4C and S5C). To get the information intuitively comparing with unweighted version, we normalize the statistics with the mean of $\sqrt{\beta_1^2+\beta_2^2}$ in baseline (eyes-closed resting state) to reasonably compare across different brain states in Figures S4C and S5C. This weighted approach enhances the effects of clear patterns and reduces the effects of ambiguous patterns. In the following analyses of EEG relative phase patterns, we find that the mode distribution can distinguish different brain states.

Furthermore, we can examine the dwell time for each mode. The dwell time refers to the time spent in a mode before transitioning to another. The mode time series changes noisily at the boundary of each mode. By investigating the average dwell time distribution across each mode, we can reduce the impact of these boundary effects and obtain a more accurate characterization of brain states. In addition, we can also define the weighted dwell time by multiplying the coefficients of multiple linear regression. Please see Figures S4C and S5C for more results from the weighted approach.

Other Measures

To validate that the relative phase approach is analogous and related to other measures, we compared it with key metrics such as amplitude and phase-lag measures. Additionally, we compared relative phase with measures that quantify traveling wave propagation to demonstrate that our measure captures the directionality of activity. To accomplish this, we applied the relative phase and other measures to the EEG data collected from the University of Michigan and looked at how the relationships between measures change across different states.

For each state, we segmented the alpha-band filtered signal into non-overlapping epochs of 2 seconds (Figure S1). The measures were then computed over these data segments. Finally, pairwise linear correlations were calculated for the time series of the measures. These correlation values were Fisher Z-transformed and averaged across subjects. P-values were calculated from these values and corrected for multiple comparisons using the Bonferroni method.

Amplitude

To calculate the amplitude, we applied the Hilbert transform to the segmented signals and averaged the instantaneous amplitude over each window. The amplitude time series for each channel was then averaged across the frontal and parietal regions. For the frontal region, we selected 14 channels corresponding to the electrodes Fpz, Fp1-2, AF3-4, AF7-8, Fz, F1-4, and F7-8. Similarly, for the parietal region, we considered the electrodes Pz, P1-8, POz, PO3-4, and PO7-8.

Phase Lag Index

As a measure of functional connectivity, we used the weighted phase-lag index (wPLI), which takes into account the strength of the phase difference between signals and is robust to volume conduction and uncorrelated noise sources.[25] The wPLI ranges from 0 (random phase lead/lag) to 1 (consistent phase lead/lag). After obtaining the wPLI matrix for all channel pairs, we averaged the values for the frontal, parietal, and fronto-parietal regions. Additionally, we introduced a directional weighted Phase Lag Index (dwPLI) as a measure of directional connectivity, computed from the signed wPLI (i.e., without taking the absolute value) and averaged across frontal and parietal channels. A positive dwPLI indicates that signals from the averaged region are phase-leading relative to other areas, whereas a negative value indicates phase-lagging.

Traveling wave propagation

We calculated two measures of traveling waves using three lines of electrodes spanning from the frontal to the occipital regions. These included one line of midline electrodes and two lines of electrodes positioned to the left and right of the midline, respectively. First, we quantified traveling wave propagation using 2D fast Fourier transform (FFT) representations of the time-by-channel data matrix.[11] The spectral peaks in the first and fourth quadrants of the 2D FFT spectra correspond to forward- or backward-propagating waves. We took the maximum value, P_{real}, over spatial frequencies in the temporal frequency domain, and repeated this procedure with shuffled electrodes to obtain a surrogate measure as P_{shuffled}. The amount of waves was then calculated in decibels [dB] as $10 \cdot \log_{10}(P_{\text{real}} / P_{\text{shuffled}})$, which represents waves relative to the null distribution. The forward- or backward-propagating waves were calculated for each electrode line, and then averaged. Additionally, we measured traveling wave propagation by calculating the phase gradient over the three lines of electrodes.[9] This involved computing the relative phase across the selected electrodes and fitting a polynomial surface to these values. For each time point, we extracted the y coefficient from the polynomial, which quantifies the phase gradient from the frontal to the occipital electrodes.

Temporal window sensitivity

We assessed sensitivity to temporal window length by repeating all comparisons across window sizes of 0.5, 2, 5, and 10 s. *K*-means clustering consistently recovered the same four canonical modes across all window sizes. Longer windows increased the dominance and dwell times of modes 1 and 4 and attenuated the transient modes 2 and 3, reinforcing that modes 1 and 4 constitute the dominant modes across temporal resolutions. Correlations between relative phase and other directional measures remained consistently high ($\varrho \geq 0.660$) regardless of window size.

Comparison between RPA and traveling-wave measures

To quantify the relationship between RPA-derived directionality and conventional traveling-wave estimates, we compared the RPA front-to-back mode coefficient $\beta_1(t)$ with the anterior–posterior phase-gradient traveling-wave measure. The traveling-wave measure was computed by estimating phase gradients along three anterior–posterior channel lines and averaging the resulting gradient time series.

We first computed the Pearson correlation between the two continuous time series to quantify their overall linear association. To examine temporal alignment and possible lead–lag relationships, we then computed the lagged cross-correlation:

$$R_{xy(\tau)} = \frac{\sum_t (x(t) - \bar{x})(y(t+\tau) - \bar{y})}{\sqrt{\sum_t (x(t) - \bar{x})^2}\sqrt{\sum_t (y(t+\tau) - \bar{y})^2}} \quad \text{(Equation 5)}$$

where $x(t)$ and $y(t)$ denote the RPA and traveling-wave time series, respectively, and τ denotes the temporal lag. Positive and negative lags were used to assess whether one measure systematically preceded the other.

Finally, to compare directional switching events directly, we transformed each continuous time series into a discrete transition-event time series. Positive-to-negative transitions were assigned -1, negative-to-positive transitions were assigned $+1$, and all non-transition time points were assigned 0. We then computed correlations and lagged cross-correlations between these transition-event time series. This analysis focuses specifically on whether RPA and phase-gradient measures identify similar directional switching events, rather than on amplitude covariation alone (Figure S1C; Table S1).

Statistical Analysis and Computational Model

In this section, we first present the details on the statistical analysis of our results, followed by the details of the computational model.

Statistics of general anesthesia analysis

To compare mode occurrences, dwell times, and iPR across different states, we performed one-way ANOVA for each mode. For each resampling iteration, confidence intervals were computed, and p-values were estimated as the proportion of bootstrap samples in which the confidence interval did not contain zero. To account for multiple comparisons, p-values were adjusted using the Bonferroni-Holm method. For the typically developed versus ADHD dataset, where the sample sizes were sufficiently large and the difference less pronounced (typically developed = 66, ADHD = 40), we conducted statistical analyses without resampling. We performed a two-sample t-test to compare mode occurrences and dwell times.

For the general anesthesia dataset, where sample sizes varied significantly across states (resting = 90, LOC = 15, Burst = 30, Suppression = 30, ROC = 45), we also applied bootstrap resampling 1,000 times per state and compared the resampled means, in addition to the regular means shown in Figures 2B and 2C of the main manuscript. The bootstrap results were highly consistent with the original analysis and are summarized as follows.

The occupancy rate of mode 1 changed from 31.02% (resting) to 32.40% (LOC), 28.48% (Burst), 14.64% (Suppression), and 23.01% (ROC). Mode 4 shifted from 28.02% (resting) to 24.31% (LOC), 23.22% (Burst), 20.03% (Suppression), and 34.49% (ROC).

Statistically significant differences in mode 1 occupancy rates were observed between resting and suppression states, resting and ROC states, LOC and suppression states, LOC and ROC states, burst and suppression states, and suppression and ROC states (one-way ANOVA test performed for all comparisons; all p-values < 0.05). For mode 4, significant differences occurred between burst and ROC states, and suppression and ROC states (all p-values< 0.05).

Mode 1 dwell time changed from 242.7 ms (resting) to 197.4 ms (LOC), 195.5 ms (Burst), 132.2 ms (Suppression), and 185.5 ms (ROC). Mode 4 dwell time varied from 224.7 ms (resting) to 179.4 ms (LOC), 173.1 ms (Burst), 148.0 ms (Suppression), and 242.8 ms (ROC). Significant differences in mode 1 dwell time were found between resting and burst states, resting and suppression states, resting and ROC states, LOC and suppression states, burst and suppression states, and suppression and ROC states (all p-values < 0.05). For mode 4, significant differences were observed between resting and suppression states, LOC and suppression states, burst and suppression states, and suppression and ROC states (all p-values < 0.001).

Statistics of ADHD analysis

For the typically developing vs. ADHD dataset (typically developing = 66, ADHD = 40), we conducted statistical analyses without resampling, using two-sample t-tests to compare mode occurrences and dwell times, with FDR correction for multiple comparisons.

Four our Receiver Operating Characteristic (ROC) curve analysis comparing the model based on Relative Phase Analysis (RPA) and the theta/beta ratio (TBR) model in individual-level diagnostic prediction (Figure 4F), we used logistic regression to determine the weights, with the diagnostic outcome as the dependent variable and the independent variables being the occurrence of mode 4, the dwell time in mode 4, and the self-transition probability from mode 4 to mode 4. We then used these weights to calculate an assessment score for each subject based on their independent variables.

Cross-band correlation analysis

To assess whether mode dynamics reflect a single broadband phenomenon or band-specific structure, we constructed a mode-transition time series for each frequency band by assigning one of the four dominant modes to each time point and computed pairwise correlations across bands. Non-adjacent frequency bands exhibited low correlations, indicating genuine frequency-specific structure, while neighboring bands showed only moderate similarity. Cross-band correlations were strongest at rest and substantially reduced under general anesthesia. The same dominant spatial mode classes were detectable across all bands, with mode-pattern correlations > 0.98, while temporal dynamics and cross-band relationships remained frequency-specific, arguing against a single broadband process.

K-means clustering method validation

Selection of $K = 4$ via Davies–Bouldin Index: To determine the optimal number of clusters for resting-state brain patterns, we evaluated clustering performance using the Davies–Bouldin Index (DBI),[93] which reflects clustering quality; lower values indicate better-separated, more compact clusters. After examining DBI values across $K = 2$ to 10, we found that $K = 4$ optimally captured the dominant relative phase patterns during the resting state.

Universality of centroids across datasets: We identified universal relative phase patterns based on resting-state data, deriving four centroids using *K*-means clustering independently from two datasets: the concatenated resting-state recordings of 18 subjects from the University of Michigan (UofM), and the concatenated resting-state recordings of the HBN control group (66 subjects). The NKI dataset was excluded due to noise introduced by simultaneous fMRI–EEG recordings. Despite different EEG systems and populations, the same four centroids emerged consistently: (i) front-leading/back-lagging (mode 1), (ii) left-leading/right-lagging (mode 2), (iii) right-leading/left-lagging (mode 3), (iv) back-leading/front-lagging (mode 4). Mode 1 and mode 4 are nearly anti-symmetric to each other, as with modes 2 and 3. These four centroids were used as the standard in all subsequent analyses.

Fuzzy C-means clustering method (FCM)

To assess whether our clustering results were robust to the use of hard assignments, we applied fuzzy *C*-means (FCM) clustering to the same relative-phase maps used in the main *K*-means analysis.[100] FCM partitions N observations $\{\boldsymbol{x}_i\}$ into K clusters by minimizing

$$J_m = \sum_{i=1}^{N}\sum_{k=1}^{K} u_{ik}^{m} \| \boldsymbol{x}_i - \boldsymbol{c}_k \|^2,$$

where u_{ik} denotes the membership of observation $\boldsymbol{x}_i$ in cluster k, $\boldsymbol{c}_k$ is the centroid of cluster k, and $m > 1$ controls the degree of fuzziness. In the present analysis, we set $m = 2$. The memberships satisfy $\sum_k u_{ik} = 1$ and $0 \le u_{ik} \le 1$. Centroids and memberships were updated iteratively according to the standard FCM update rules:

$$\boldsymbol{c}_k = \frac{\sum_i u_{ik}^{m} \boldsymbol{X}_i}{\sum_i u_{ik}^{m}}, u_{ik} = \left[\sum_{j-1}^{K} \left(\frac{\|\boldsymbol{X}_i - \boldsymbol{c}_k\|}{\|\boldsymbol{X}_i - \boldsymbol{c}_j\|}\right)^{\frac{2}{m-1}}\right]^{-1}$$

We applied FCM to the eyes-closed data from 18 subjects from the University of Michigan dataset and evaluated K over the same range used in the hard-clustering analysis (Figures S3A and S3B). FCM recovered centroids closely matching the K-means modes and supported the same optimal $K = 4$. Modes 1 and 4 were nearly identical across methods ($\varrho > 0.99$), whereas the transient modes 2 and 3 showed lower but still high correlations (> 0.66). When each time point was assigned to the mode with the highest FCM membership, 85.46% received the same label as in K-means, confirming the robustness of the hard-assignment approach.

Simulation of relative phase dynamics with Kuramoto model

To elucidate the mechanism behind the mode fluctuations, we ran simulations of relative phase dynamics using a Kuramoto model, a well-known canonical coupled oscillator model frequently used to model large-scale cortical dynamics.[7,29,101–114] Using the generated relative phase signals from the model on human cortical network, we constructed the spatially extrapolated relative phase topographic map to obtain regression coefficients (β_1 and β_2) that specify the mode distribution over different brain states, using the same procedure for the empirical EEG data. Specifically, we focused on modeling the general anesthesia EEG data (UofM, University of Michigan) to find the model parameters that best match the empirical statistics of the brain states including mode occurrence and dwell time.

Structural connectivity data. The structural and function connectome data was collected from 70 healthy individuals on a 3T scanner.[115] We used a group-averaged structural network generated with a consensus approach[116] which preserve the edge length distribution in individual participants, described in detail elsewhere.[48,117,118] In particular, we used the network with 114 regions. The structural matrix was further binarized, yielding a binary adjacency matrix of size 114 by 114 specifying the connectivity between brain regions (represented by the matrix A_{ij} in Figure 5). This matrix was then used to specify the connection between nodes in the Kuramoto model, explained below.

Kuramoto model. To simulate the phase signals of individual regions on the brain network, we utilized a Kuramoto model with a generalized coupling function that includes a constant term (c_0), which results in a more realistic first order approximation of many coupling functions obtained from the phase reduction method.[32,33,119] The model is written as:

$$\frac{d\theta_i}{dt} = \omega_i + S\sum_{j=1}^{N} A_{ij}\left[c_0 + \sin\left(\theta_j - \theta_i - \tau\right)\right], \qquad \text{(Equation 6)}$$

where θ_i is the phase of the oscillator i, ω_i is the intrinsic frequency of the oscillator, S is the global coupling strength, $\boldsymbol{A}$ is the binary adjacency matrix of the network (1 if connection exists between node i and j, 0 otherwise), and τ is the phase shift term between two nodes capturing the transmission delay between regions. c_0 is a constant that results from the first-order approximation of the coupling function. Seen in another way, this term can be thought of as a natural consequence of incorporating diffusive coupling in limit cycle oscillators.[36,67,68,70] For all of our simulations, we set $\omega = 10$Hz for all nodes to focus on the alpha band frequency, and $\tau = 0.12\pi$, which approximately translates into the average time delay between brain regions.

Ornstein-Uhlenbeck (OU) and other stochastic processes in c_0. The previous study has shown that inclusion of the c_0 parameter in the coupling function of oscillators results in a rich repertoire of phase dynamics, especially relevant to the transitions between two distinct and dominant modes in the brain: one in which high-degree midline cortical regions phase-lag the network becoming sink of the directionality, and one in which they phase-lead the network and becoming source of the directionality.[68] To simulate the signals, we assumed that the brain exhibits random fluctuations in the c_0 parameter. The stochastic dynamics were specified with the Ornstein-Uhlenbeck (OU) process,[120] a commonly adopted framework for implementing time-varying random noise.[121–125] Formally, the OU process for our variable of interest x_t ($= c_0$ at time t) is described as:

$$dx_t = -\psi(x_t - \mu)dt + \sigma dW_t, \quad \text{(Equation 7)}$$

where ψ is the parameter controlling for the rate of drift toward the constant μ which specifies the mean of the process, and σ is the parameter controlling the variance of the Gaussian noise dW_t. While μ could be a free parameter, we set $\mu = \sin(\tau)$ for all simulations as this corresponds to the in-phase synchronous state.

To explore other potential random dynamics in c_0 that might account for the observed relative phase dynamics, we tested two additional stochastic processes involving pitchfork bifurcations. More specifically, the *supercritical* case was described by its normal form involving third-order term, with the variable centered at μ as follows:

$$dx_t = -\psi\left(r(x_t - \mu) - (x - \mu)^3\right)dt + \sigma dW_t, \quad \text{(Equation 8)}$$

where $r > 0$ is the parameter controlling the distance between the two stable fixed points (Figure S6B). Note that the two stable fixed points appear only when $r > 0$.[126]

For the *subcritical* case, an additional fifth-order term was included to stabilize the dynamics as follows:

$$dx_t = -\psi\left(r(x_t - \mu) + (x - \mu)^3 - (x - \mu)^5\right)dt + \sigma dW_t, \quad \text{(Equation 9)}$$

where r is a parameter bounded between $-0.25 < r < 0$ to allow for two stable fixed points (Figure S6B). For all simulations, we chose $r = 0.1$ for the supercritical case and $r = -0.18$ for the subcritical case to allow for two stable fixed points on both sides of $\mu = \sin(c_0)$, namely, the attractors states for mode 1 and 4 (Figure S6A).

Parameter estimation using grid search. To estimate the parameters of the stochastic processes, we ran simulations of Kuramoto oscillators with stochastic processes in c_0 for 60s with a time step of $\Delta t = 0.001$ (for a total of 60,000 time steps). This was repeated for 10 unique random seeds, and the resulting mode occurrences and dwell time were averaged. We used grid search to run simulations with the given values of ψ, σ (step size of 0.5), and the coupling strength S (step size of 0.1), and selected the set of parameters which exhibited the minimum mean absolute error from the empirical mode occurrences and dwell times.